" COMMISSIONING AND CHARACTERIZATION OF THE MANITOBA
AUTOMATED HIGH ENERGY PROTON MICROPROBE, AND THE
ROLE OF COLD AND HOT FUSION IN THE IMPLANTATION
OF PALLADIUM AND INDIUM BY DEUTERONS"

BY

YOU HUAN YEO

A THESIS

Submitted to the Faculty of Graduate Studies in Partial
Fulfilment of the Requirements for the Degree of

MASTER OF SCIENCE

Department of Physics
University of Manitoba
Winnipeg, Manitoba

OCT 1989

Canada

COMMISSIONING AND CHARACTERIZATION OF THE MANITOBA
AUTOMATED HIGH ENERGY PROTON MICROPROBE, AND THE ROLE OF
COLD AND HOT FUSION IN THE IMPLANTATION OF PALLADIUM
AND INDIUM BY DEUTERONS

BY

YOU HUAN YEO

A thesis submitted to the Faculty of Graduate Studies of
the University of Manitoba in partial fulfillment of the requirements
of the degree of

MASTER OF SCIENCE

© 1989

Abstract

A high energy proton microprobe has been constructed on
a dedicated beamline at the University of Manitoba
Accelerator Centre. Chapter one describes the extensive
program of design and development of the major components of
the microprobe. These developments include the design of the
target chamber, the object slit and the beam scanning stage.
The performance of the major components and the overall
system to date is assessed.

Chapter two describes the experiment involving the
implantation of deuterons into the palladium and indium
targets. This experiment was designed to observed the
possible neutrons resulting from the so-called 'cold fusion'
effect when there is a sufficiently high concentration of
deuterium nuclei present in the target samples. The
motivation was to simulate the Utah electrolysis experiment
in a non-equilibrium situation not involving heavy water as
the intermediate material. A significant neutron production
was observed in the implantation experiment and a preliminary
examination on the role of 'cold' and 'hot' fusion in this
experiment is described.

Acknowledgements

Table of Contents

Chapter One

Commissioning and Characterization of the Manitoba Automated

High Energy Proton Microprobe

1.1 Introduction

A proton microprobe is an instrument used for the microanalysis of a sample in which a beam of protons is focussed onto a target area of micrometer dimensions. As of 1988, some fifty proton microprobe facilities had been developed [1]. This list includes a new and unique device, the Manitoba Automated High Energy Microprobe (MA-HEM) which has recently been completed at the University of Manitoba Accelerator Centre. It uses the spiral ridge cyclotron as the particle source. The Manitoba high energy microprobe operates at a proton energy of 40 MeV and yields a beam spot approximately 10 μm in diameter. This microprobe is designed to exploit features not available to microprobes operating at a few MeV incident proton energy. Because 40 MeV protons have a considerably larger range in matter and a lower energy loss as compared to low energy protons (1-5 MeV), MA-HEM is an ideal instrument for thin sample transmission microanalysis. Also at 40 MeV, the yield for K x-ray production is at or near its maximum value for most rare earth and medium to large Z heavy elements [2,3]. MA-HEM can measure elemental concentrations at the 1 ppm level for all elements from arsenic to uranium in the periodic table. This level is a factor of 100 times lower than that obtained by low energy proton microprobes and 1000 times lower than

that reached by scanning electron microscopes.

When used in conjunction with the proton induced x-ray emission (PIXE) technique, MA-HEM becomes a microscope able to examine the details of elemental composition of geological samples at the inclusion level, biological samples at the cellular level and physical samples at the micron level.

1.2 Description of MA-HEM Assembly

The schematic layout for MA-HEM is shown in Figure 1.2.1. The 40 MeV proton beam leaves the cyclotron through a slit of dimensions 5 mm x 12 mm in the x- and y- directions respectively. The direction of propagation of the beam is along the z-axis. It is first focussed by a preconditioning magnetic quadrupole doublet (Q_a, Q_b) to produce an image at the 70 μm x 70 μm microprobe object slit, 5.49 m downstream from the cyclotron exit slit. Each of the preconditioning quadrupoles has a half aperture of 5.27 cm and an effective length of 31.1 cm. Tne first quadrupole defocusses the beam in the x-z plane and focusses it in the y-z plane. The second quadrupole focusses the beam in the x-z plane and defocusses it in the y-z plane. The operating conditions for Q_a and Q_b are 276 mT and 278 mT respectively.

Another system of four magnetic quadrupoles (Q_1, Q_2, Q_3, Q_4), is placed 1.8 m further downstream from the microprobe object collimation slit. Each of the four quadrupoles has an aperture diameter, pole tip to pole tip, of 5.08 cm and an effective length of 21.15 cm. Neighbouring quadrupole magnets are separated by 8 cm. The first and fourth quadrupoles (outer doublet) have equal but opposite fields, as have the second and third doublet (inner doublet). The

inner doublet is oriented at 90° relative to the outer

doublet. The pole tip magnetic field for the inner doublet

is 599 mT, and 286 mT for the outer doublet. This CDCD[1] (in

x-z plane), or DCDC (in y-z plane) configuration, is commonly

referred to as a 'Russian quadruplet' [4]. This set of

quadrupoles will then focus the proton beam emerging from the

object collimation slit to an image spot 10 μm in diameter at

a distance of 20 cm from the exit of the fourth magnet of the

quadruplet system. A beam current at the sample of 300 pA

per μA extracted from the accelerator, is measured by means

of a secondary electron emission monitor placed 0.5 m from

the focus of the microprobe.

---

[1]C: Converging, D: Diverging
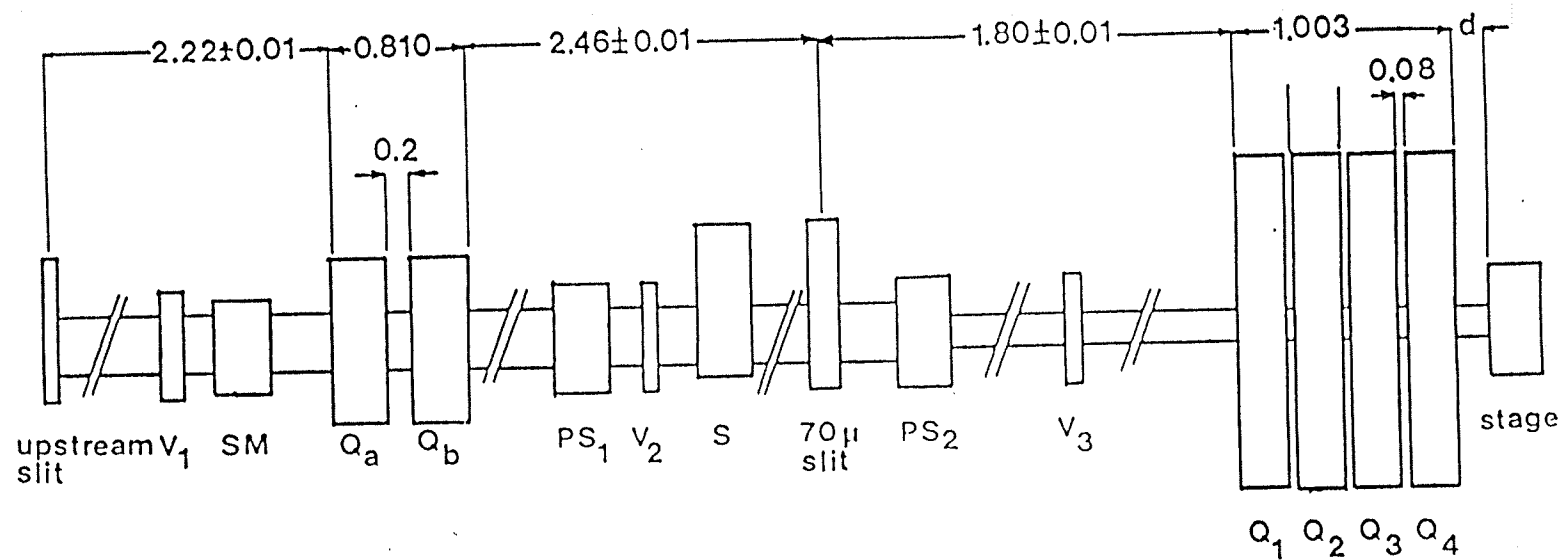
Figure 1.2.1 Schematic layout of the MA-HEM assembly. V_1, V_2
and V_3 are vacuum valves, PS_1 and PS_2 are
pumping stations, S is the viewing screen and
the final image point is at a distance d=0.20 m
behind the limits of Q_4.

1.3 Optimization and Alignment

1.3.1 The Object Slit

The object slits of a microbeam system are crucial to the attainment of small spot size. The MA-HEM Object collimation slits were constructed from stainless steel. This collimator design incorporates two crossed slits with entrance and exit angles of 15° and 2° respectively [5]. The slit design is shown schematically in Figure 1.3.1, where R represents the proton range in steel. The entrance and exit angles are also indicated.

A laser diffraction technique was used to calibrate the MA-HEM object slit. The experimental set-up is shown in Figure 1.3.2. A He-Ne laser with wavelength 632.8 nm was used. By observing the interference pattern on the screen which resulted from a laser beam incident on the object slit, the dimensions of the slit are calculated using the following equations [6],

$$a = (m+1/2)\lambda r/x$$

$$b = (n+1/2)\lambda r/y$$

15°

2°

70 μ Nobiling
slit design
for MA-HEM

R
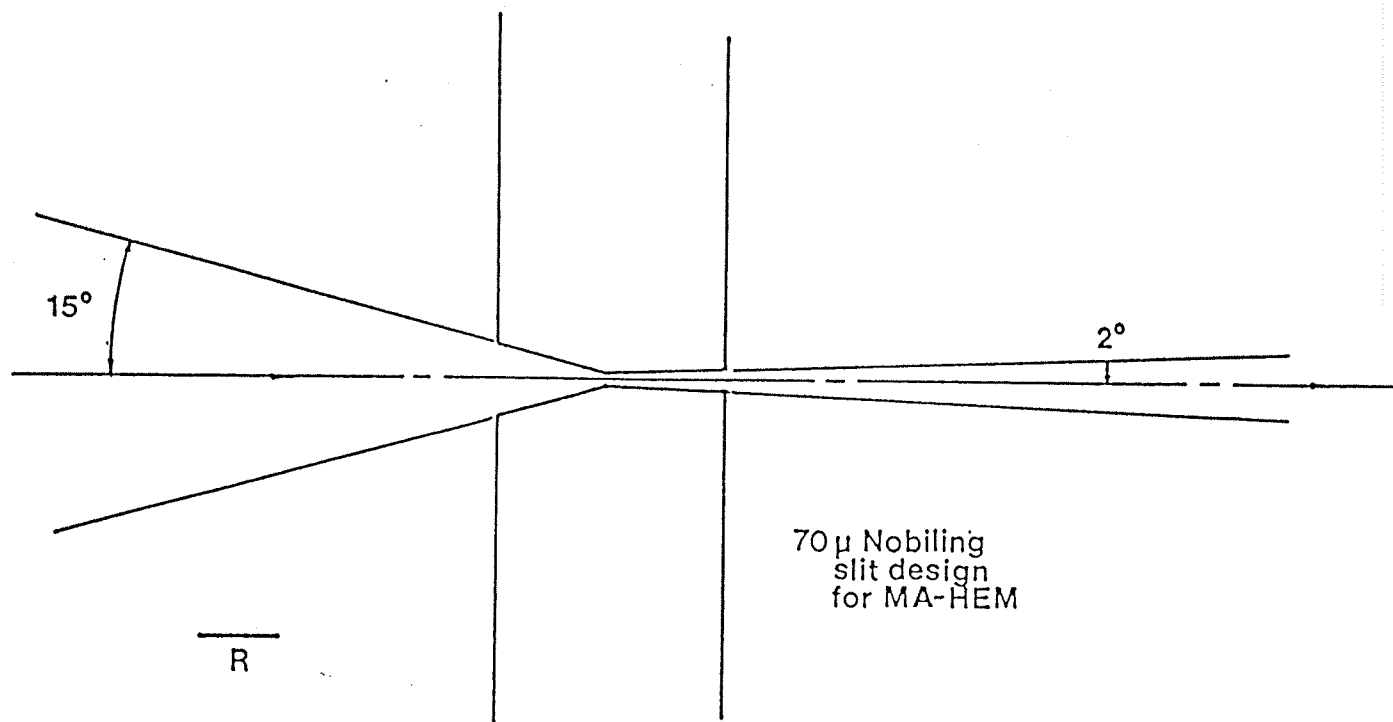
Figure 1.3.1   The MA-HEM object slit, where R is the proton

range in steel.
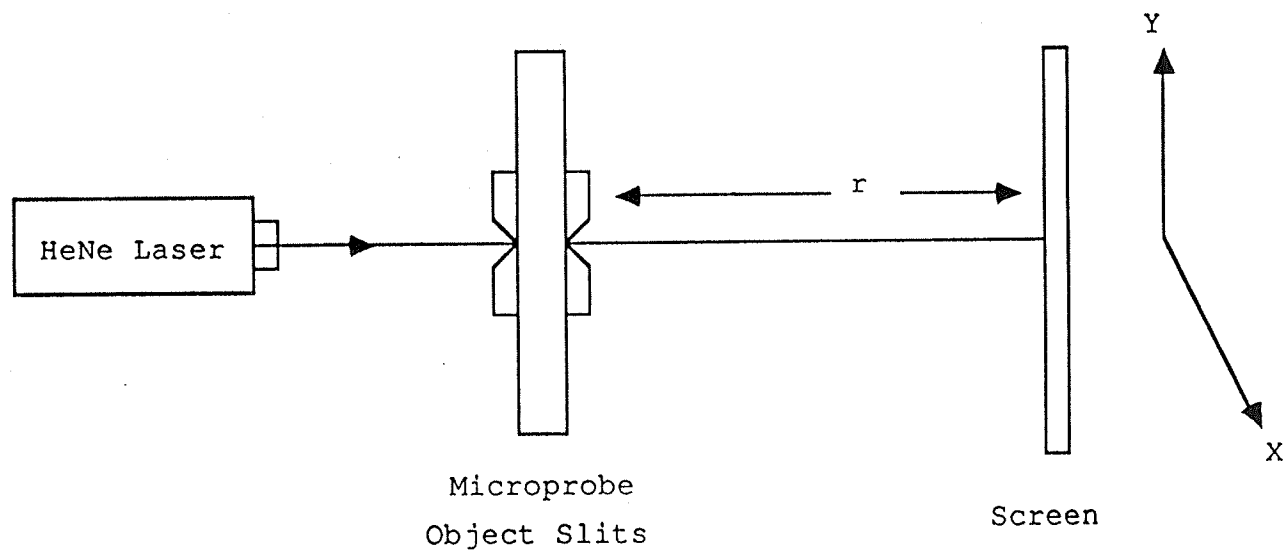
Figure 1.3.2 Experimental setup for calibration of the

microprobe object slit.

where a and b are the half dimensions of the object slit.
In this case, the MA-HEM object slit was determined to have
dimensions of 2a=(72 +/- 2) μm and 2b=(72 +/- 2) μm.

1.3.2   The 'Russian quadruplet'

The critical components of the focusing system are the
slit used to define the object aperture, and the magnetic
lens system used.

The microprobe quadrupole lenses were designed to
minimize surface roughness of the pole tips which ensures
uniformity of the magnetic field and minimizes parasitic
aberrations. Figure 1.3.3 shows the cross sectional geometry
of the quadrupole lens used. These microprobe quadrupoles
exhibit excellent differential linearity in the central 30 mm
of the magnet bore, as shown in Figure 1.3.4.

The magnetic field mapping of the 'Russian quadruplet'
was done using a Bell 640 incremental Gaussmeter and a
transverse probe. The dimensions of the probe are l=25.4 mm,
w=3.7 mm and h=1 mm. A 2 m long plastic tube was designed to
hold the probe during the magnetic field measurement. The
transverse probe was placed at 1.43 cm from the centre of the
magnet bore. The magnetic field was then measured as a
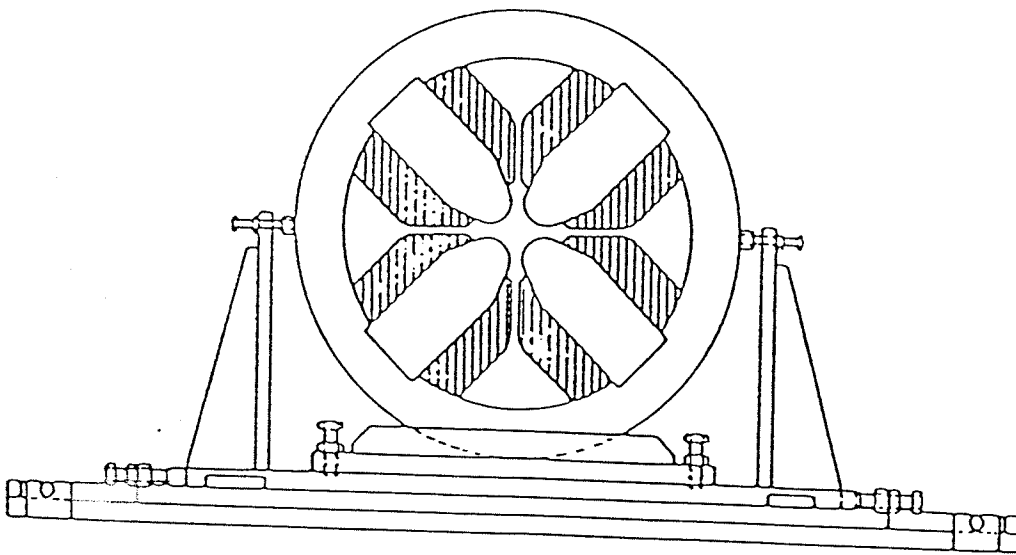
Figure 1.3.3   The cross sectional geometry of the quadrupole

lens used.
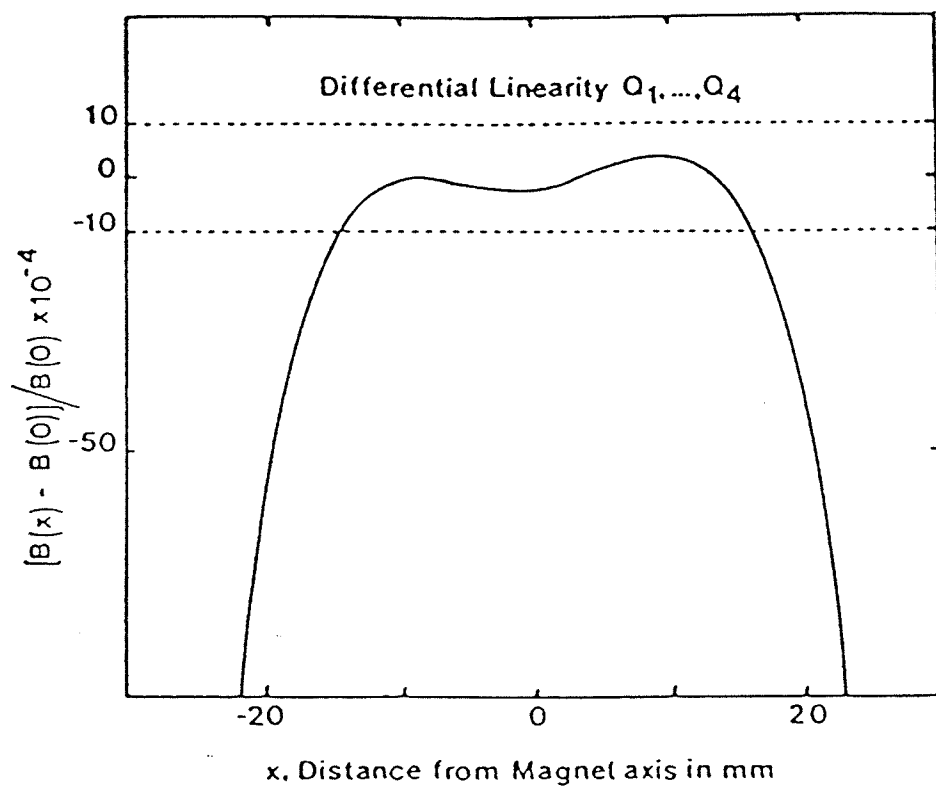
Figure 1.3.4   Differential linearity of microprobe quadrupoles.

function of the current applied to the magnet coils. All the measurements were done in the region where the magnetic field strength is a maximum. Figure 1.3.5(a), (b), (c), (d) show the variation of the field strength with current for all four quadrupole magnets. The relationship between the field strength and current is linear, as expected.

The average B field measured at 100 A for the quadruplet system is (305 +/- 3) mT. The operating condition for the quadrupole requires 599.1 mT at the pole tip for a 100 A excitation current. A simple calculation shows that this requirement is satisfied by the measured value. The uncertainty in the field results from two sources: First the tranverse probe is of finite size. Thus the measured values of the B-field are averaged over the area of the transverse probe; and secondly there is always the possibility of a misalignment of the quadruplet system.

1.3.3 Alignment

The slit, quadrupole magnets and target chamber must be located relative to the design axis of the beam from the accelerator. This can be done using conventional surveying techniques involving alignment lasers, telescopes and/or a theodolyte. The Manitoba microprobe system was aligned using

a theodolyte. The optical axis of the system is taken to be the path of a particle which passes through the tip of a defining spire placed in the switching magnet, the centre of the object slit and a fiducial point on the microprobe-line aligning wall plate.
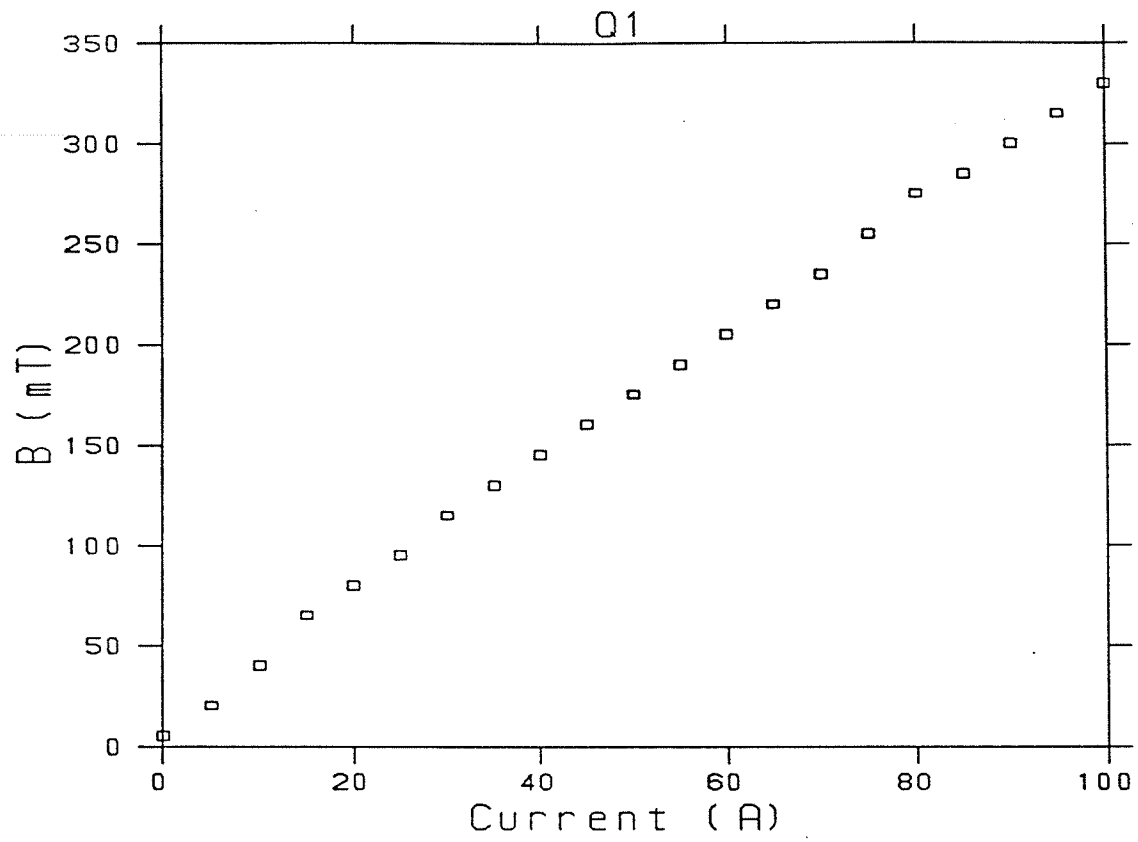
Figure 1.3.5(a)   Relationship between field strength and

current for Q_1.
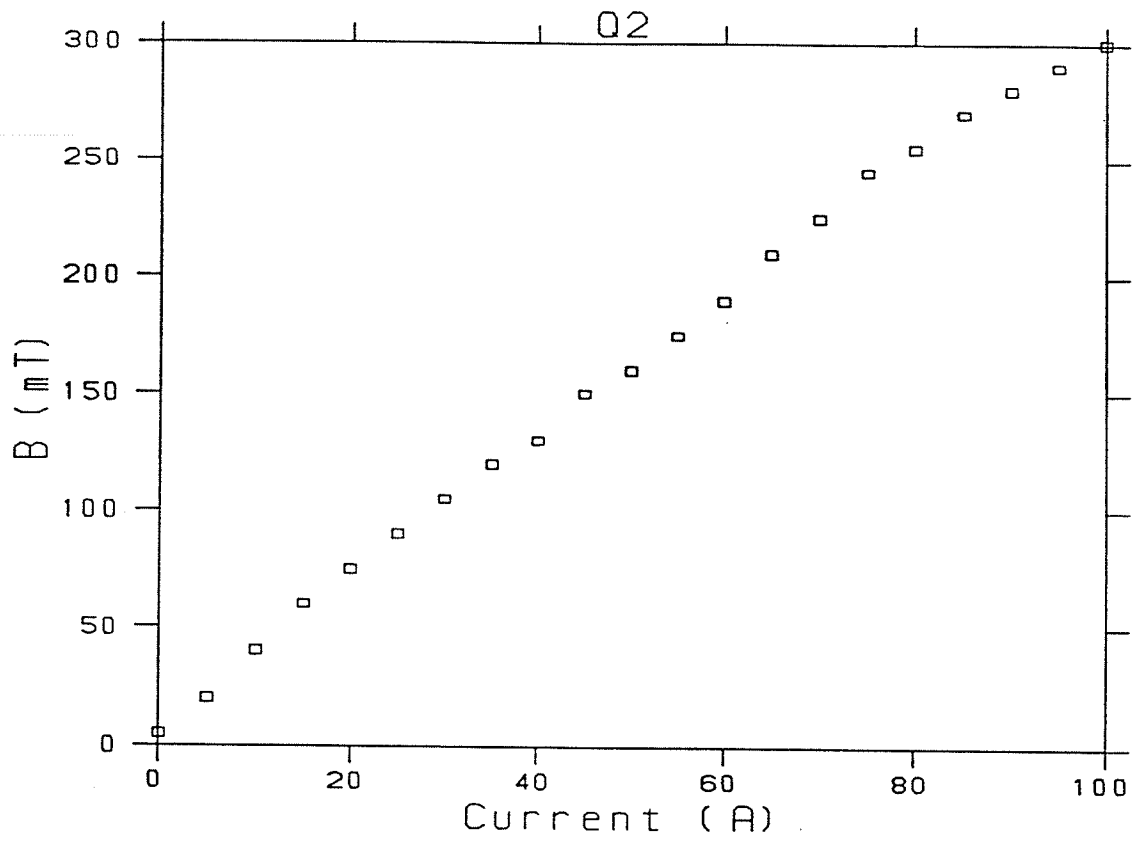
Figure 1.3.5(b)   Relationship between field strength and
current for Q_2.
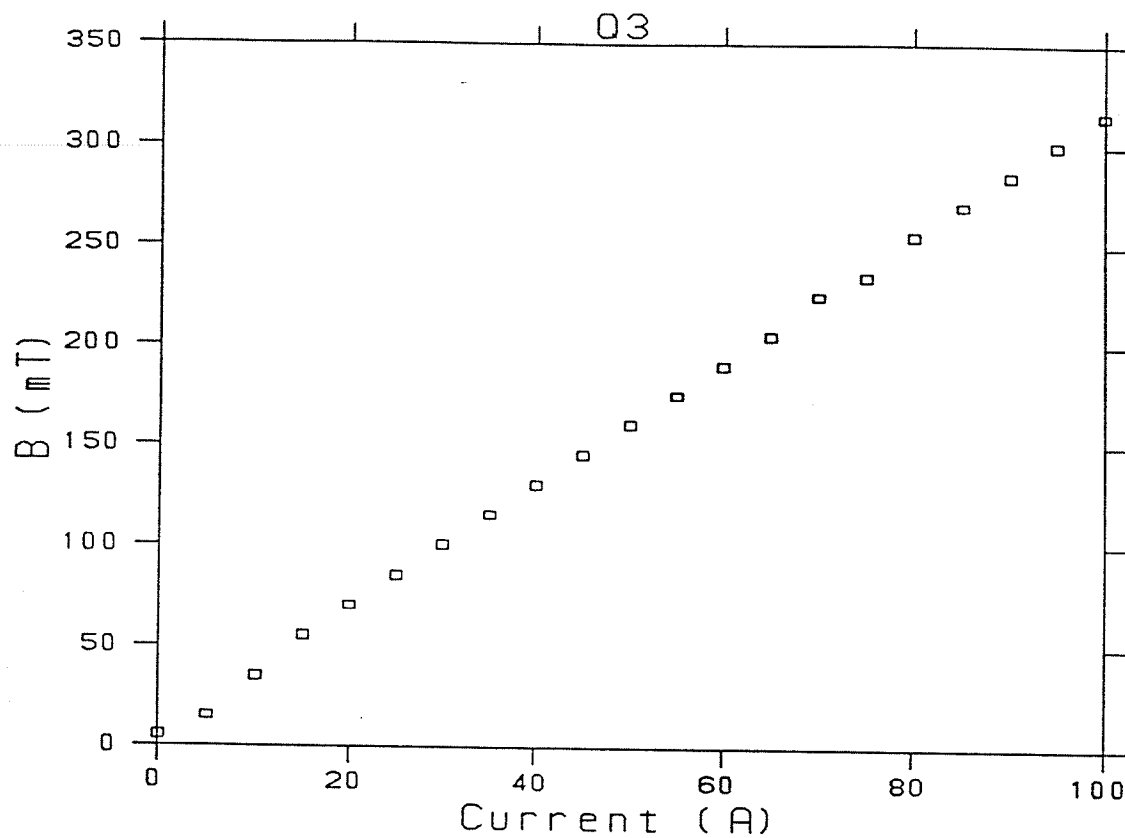
Figure 1.3.5(c)   Relationship between field strength and
current for Q_3.
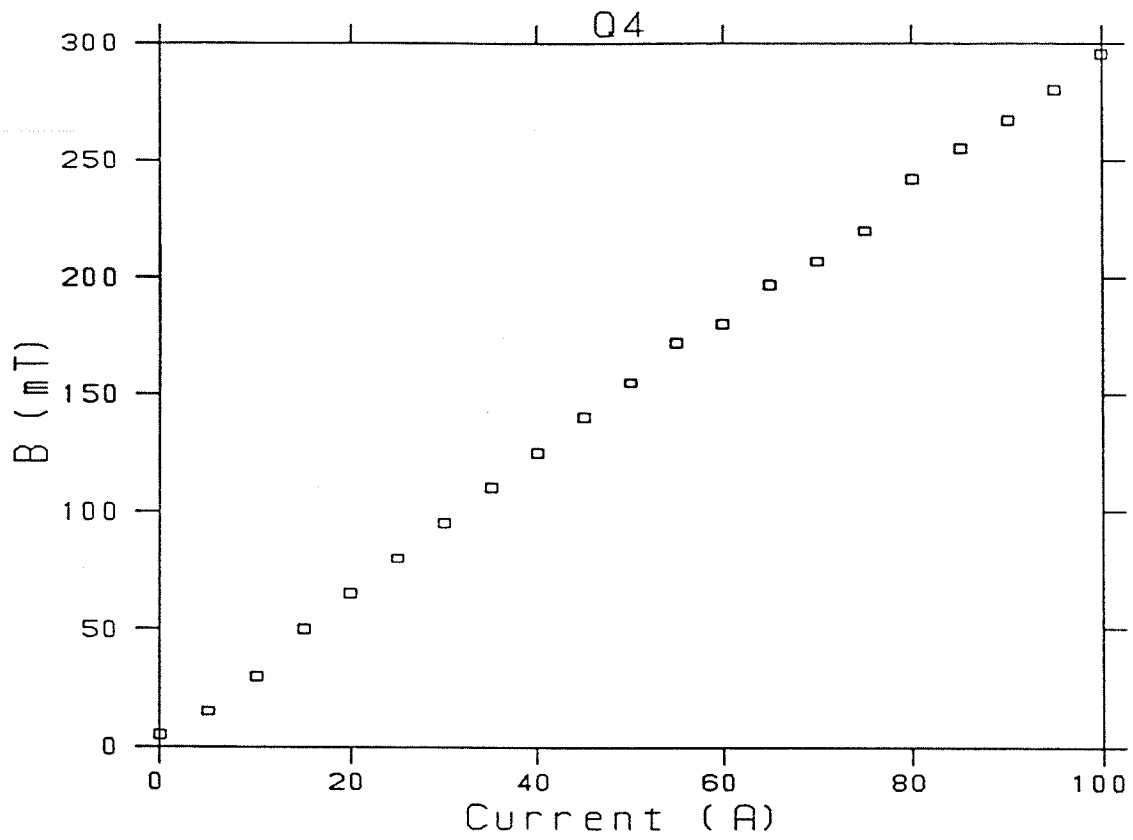
Figure 1.3.5(d)   Relationship between field strength and current for Q_4.

1.4 <u>Preliminary Study</u>

Focusing a 70 μm diameter spot from the object collimation slit to a 10 μm spot at the sample requires a demagnification factor of 7 and the attainment of magnetic field strengths in the 'Russian quadruplet' as mentioned earlier.

Replacing the 70 μm x 70 μm slit with a 3 mm diameter carbon collimator enables a visual examination of the final beam spot using a phosphor screen as the beam passes through the microprobe lens system. A 40 MeV beam spot of roughly 2 mm in diameter was observed visually on the phosphor screen located at the focus of the microprobe. Since previous measurements indicate that the actual beam size is roughly 1/5 the observed size due to the multiple scattering of the proton beam on the phosphor screen, the actual beam spot size observed is then roughly 0.4 mm. This implies that a demagnification factor of 7 is achieved from the 'object' to 'image' for the microprobe focusing system. This is the first experimental verification of a design parameter for MA-HEM [7].

The next task was to install the 70 μm x 70 μm object slit into the microprobe beam line. A wall of concrete

blocks was erected between the object slit and quadruplet system to attenuate background radiation coming from the upstream portion of the beam line and arriving at the target stage.

A 125 μm thick lead sheet was then placed at the focus of the microprobe. Using the PIXE technique, an experiment was performed for a run time of 30 min. A standard ^{241}Am source was used to calibrate the HpGe solid state detector. Figure 1.4.1 shows the effect of a 40 MeV, unfocussed 70 pA microbeam on the lead sheet. Four clearly distinguishable K x-ray lines from the lead were observed. This result confirms the transportation of a microbeam from the object slit to the focal point of the microprobe assembly.

It is useful to obtain a preliminary knowledge of the dimensions of the beam spot prior to subsequent use of the microprobe. A piece of thin mylar was placed at the focus of the microprobe and irradiated with a 40 MeV microbeam for approximately 3 hours. The size of the resultant beam spot was measured to be roughly 100 μm in the vertical direction and 50 μm in the horizontal direction. The final measurements were made using a travelling microscope.

The fact that the spot size measured here is larger than
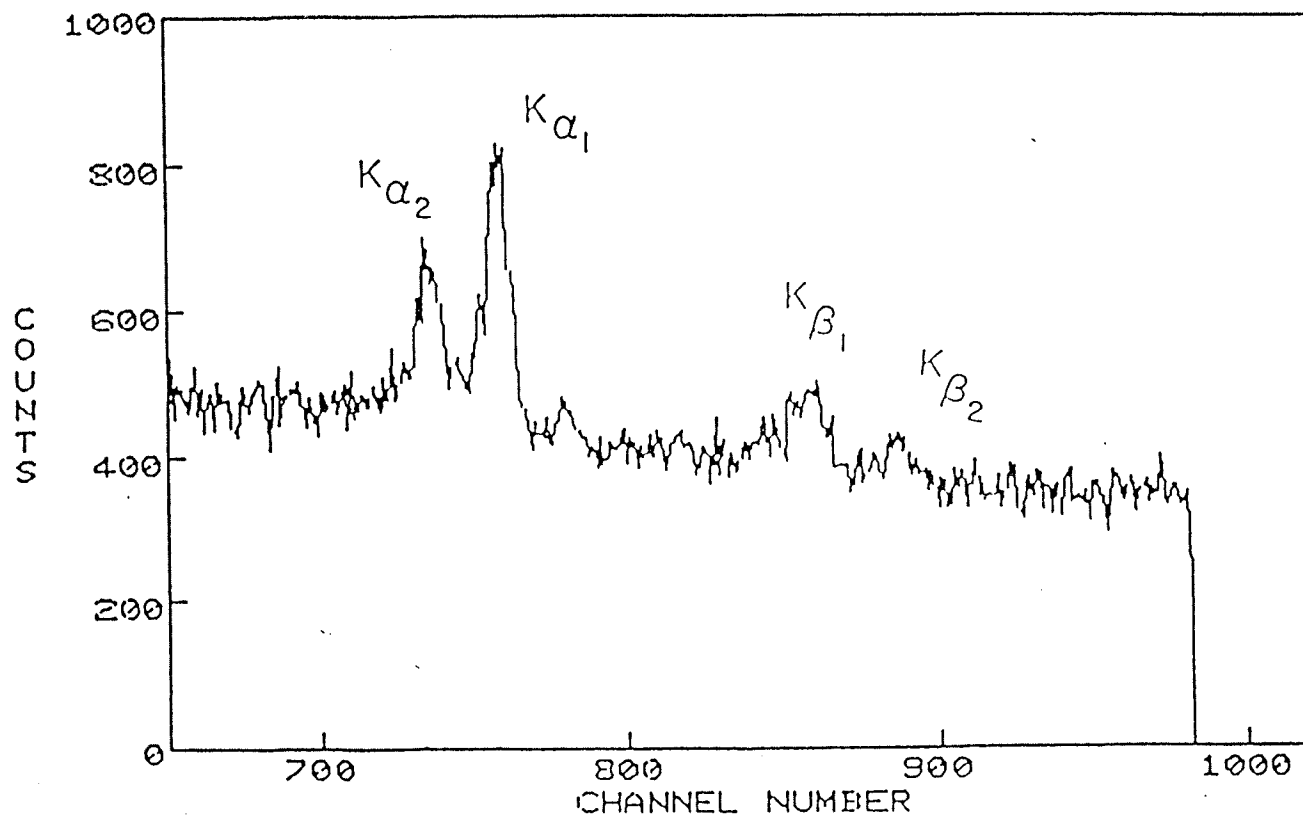
Figure 1.4.1 Raw data from a 125 μm lead target bombarded by an unfocussed 40 MeV, 70 pA proton beam.

the anticipated instantaneous 10 μm dimension is due to the nature of this measurement and to factors involving long term beam stability and mechanical vibration. A granite table and isolation bellows have now been acquired which it is believed will solve this problem. Feedback of current information through use of a downstream split-ionization chamber for example, may be advisable in the future for routine automatic operation. The accurate measurement of the instantaneous spot diameter can however now be made, and details of that technique are given in the paragraphs which follow.

1.5 Measurement of the Spot Diameter

1.5.1 Introduction

The spot size of a microbeam system is usually determined by sweeping the beam over a sharp edge such as an evaporated strip of metal, a fine wire or the bars of a microscopic mesh [8], and recording the PIXE signal from the metal as a function of the position of the target. The spot size can then be determined from the range of positions over which the signal increases. This process must be repeated with the target moving in the other direction, perpendicular to the first, to obtain the dimensions of the spot in both x- and y- directions. In the early days of low energy proton microprobe development, optical objective lenses were used to magnify the microbeam spot so that its dimensions could be studied by measurement on a projected screen. This method is, however highly expensive and inappropriate for a high energy microbeam.

1.5.2 MA-HEM Beam Scanning Stage

The measurement of the dimensions of a high energy proton microbeam is far from simple task. Because of the overall radiation field in the vicinity of the target stage,

remote monitoring of the beam and its interaction with matter is essential. A television camera provides a means of monitoring experimental conditions visually. The method chosen for measuring the beam spot of MA-HEM is as follows [9]. A 10 or 20 μm tungsten wire is moved perpendicularly and horizontally across the beam at the focus of the microprobe. Interaction of the microbeam with the tungsten wire results in the production of tungsten K x-rays. These K x-rays are then detected by a HpGe detector and their intensity is recorded as a function of the position of the wire. The dimensions of the beam spot can then be obtained by identifying the full width at half height in the resulting profile [10].

As a means of moving the wire, it was decided that a digitally controlled stepping motor would be most suitable. The schematic layout of the scanning stage is shown in Figure 1.5.1. Simplicity and precision were the reasons for choosing the worm gear coupled to a rack and pinion for the transmission of motion. The tungsten wire is mounted (glued with epoxy) across a 'C' shaped metal frame. This is in turn connected to a rod passing through the target chamber wall by means of a double O-ring seal. The rod is then bolted to the rack.
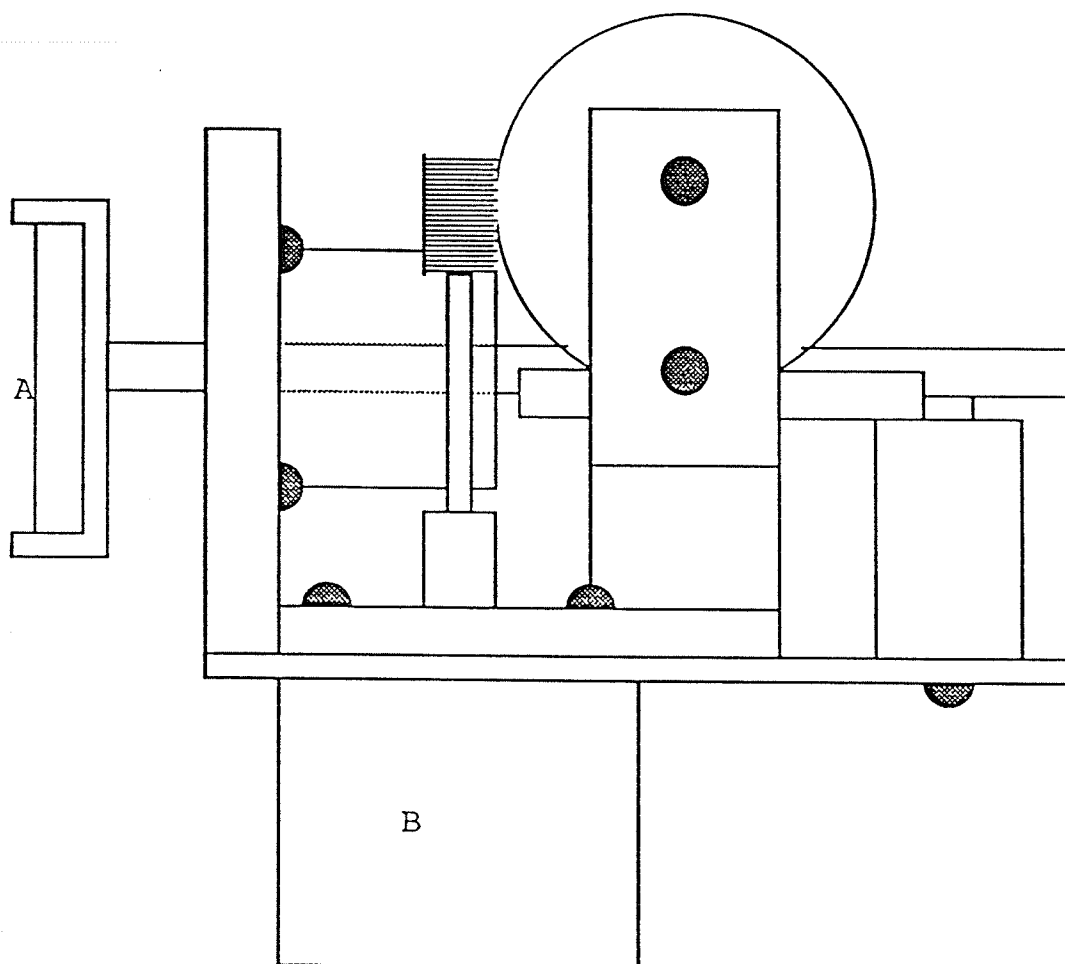
Figure 1.5.1   Schematic diagram of MA-HEM beam scanning stage

where A: 10 or 20 μm tungsten wire

B: Stepping Motor.

The target chamber is cylindrical, machined from a
aluminum pipe six inches in outer diameter and five inches in
inner diameter. Two, one inch wide horizontal slots which
allow passage of x-rays, are cut along an arc of the cylinder
and covered with the x-ray transparent material, kapton.
Both HpGe and SiLi detectors may then be positioned at these
two slots, which are 45° to the beam axis.

The movement of the stepping motor is controlled
remotely by a set of electronic hardware situated in the
cyclotron control room. A schematic layout of these pieces
of hardware is shown in Figure 1.5.2.

A Chronetics pulser is used to generate a time base for
the stepping motor controller. Each pulse causes the MBD to
perform a time related function such as pulsing the motor.
The function of the LRS3511 ADC is to notify the MBD that a
time base pulse has occured. An Input Gate-Output Register,
'IGOR' is used to control both the direction and movement of
the motor. The MBD, and thus the VAX has complete control of
the stepping motor. The overall scanning system has been
completed and is operational.

For every step of the motor, the tungsten wire will move
an increment of 0.5 μm. A PIXE experiment will then be

```
┌─────────────┐          ┌────────┐          ┌────────┐      ┌────────┐
│  Stepping   │          │        │          │        │      │        │
│             ├──────────┤  IGOR  ├────┬─────┤  MBD   ├──────┤  VAX   │
│   Motor     │          │        │    │     │        │      │        │
└─────────────┘          └────────┘    │     └────────┘      └────────┘
                                       │
┌─────────────┐          ┌────────┐    │
│ Chronetics  │          │        │    │
│             ├──────────┤  ADC   ├────┘
│   Pulser    │          │        │
└─────────────┘          └────────┘
```
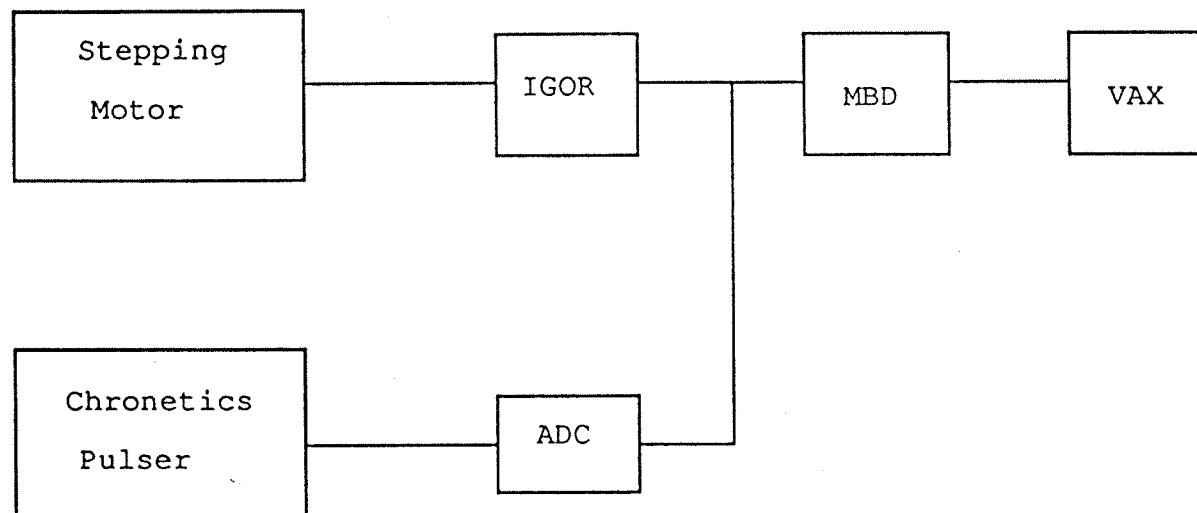
Figure 1.5.2   Schematic drawing of the electronic hardware

used to control the scanning stage.

performed at this position and the intensity of the resulting
x-rays recorded. This procedure is repeated until a profile
is obtained and analysis of this profile will yield the
dimensions of the beam.

1.6 Future Work

1.6.1 Alignment of the 'Russian quadruplet'

Parasitic aberrations of a focusing system are largely due to imperfect alignment of the lens relative to the beam axis. Three common mechanical misalignments of a quadrupole lens are: transverse displacement of the lens, tilting of the lens and rotation of the lens about the beam axis. These misalignments will cause parasitic aberrations which result in degrading the size of the final beam spot [11]. Hence proper alignment of the lens system is required prior to detailed investigation of the beam spot size.

1.6.2 Quadrupole Power Supply

To avoid degrading the focus of the final beam spot due to field fluctuations, the power supplies used to excite the magnet coils should have sufficient stability and precision. In practice, the current applied to the magnet coils is required to be stable to the order of 1 part in 10^5 or better.

The power supply currently used for the outer doublet of the MA-HEM quadruplet has a stability of 1 part in 10^3, while

the supply for the inner doublet has a stability of 1 part in 10^5. In order to achieve a fine focus of the microbeam, it is required that the existing power supply for the outer doublet be replaced by a high stability constant current supply.

1.6.3 Vibration Isolation

It is important to ensure that the target chamber does not move relative to the microbeam during the analysis of the beam spot or samples. The most likely cause of target chamber movement is building and pump vibration transmitted to the target stage through the equipment supports. Any vibrating equipment associated with the target chamber, such as vacuum pumps, needs to be well isolated from the target/magnet system.

As of today, the MA-HEM target stage is not isolated from vibrations. This implies that the results of the preliminary measurement of the beam spot using the thin mylar is not 'vibration free'. Hence the actual beam spot is most probably much smaller than the measured dimensions when vibration is taken into account. To further the study on the nature of the beam spot, it is suggested that the target chamber be isolated from the vibrating equipments with anti

-vibration mountings and flexible connections.

1.7 Conclusions

In conclusion, a proton microprobe operating at 40 MeV has been constructed. Preliminary results show good agreement with the design parameters. The performance of the major components of the microprobe and the overall system is as expected. Time and financial contraints have prevented the scanning of the beam spot using the newly designed scanning stage. However, it is expected that the beam spot size is roughly 10-20 μm in diameter when all the necessary improvements to the system, such as those mentioned in the last section, have been completed.

Chapter Two

The Role of Cold and Hot Fusion in the Implantation of
Palladium and Indium by Deuterons.

2.1 Introduction and Motivation

Nuclear fusion is a process involving the combination of two light nuclei to form a heavier nucleus. It is well known that fusion of isotropic hydrogen is an efficient mechanism for energy production. In the case of two deuterium nuclei, in order for the two nuclei to come sufficiently close together to interact, they must first either pass over or tunnel through the Coulomb barrier. For 40 years, it has been believed that such a fusion process is only possible in an environment of temperature in excess of a million degrees.

The Deuterium fusion reaction includes:

$$D + D \longrightarrow {}^3He + n + 3.2 \text{ MeV}$$

$$D + D \longrightarrow T + p + 4.0 \text{ MeV}$$

$$D + T \longrightarrow {}^4He + n + 17.6 \text{ MeV}$$

$$D + {}^3He \longrightarrow {}^4He + p + 18.3 \text{ MeV}$$
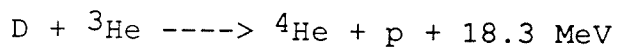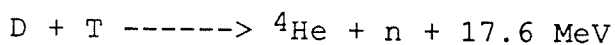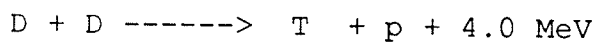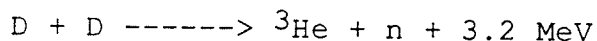
The first two reactions indicate that the D-D fusion can follow either of two paths, either producing helium-3 and a neutron or tritium and a proton. Both of these reactions are equally probable. The heavy products of the first two reactions become reactants in the third and fourth reactions. The entire reaction

$$D + D \longrightarrow {}^4He + p + n + energy$$
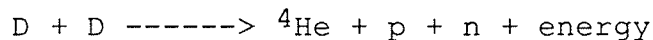
results in a net release of energy of 21.5 MeV.

Cold fusion which takes place at room temperature is possible. One mechanism for cold fusion involves replacing the electron in a $D_2{}^+$ molecule by a negative muon [12]. The more massive particle reduces the separation between the two deuterium nuclei by a factor 200, and consequently increases the neutron tunnelling probability by about 85 orders of magnitude over that expected for a normal molecule.

Another approach to the phenomenon of cold fusion has recently been studied in some detail by Fleischman and Pons [13] and Jones et al. [14]. Both groups employed a conventional electrolytic cell with a platinum anode surrounding a palladium cathode. The electrolyte of the cell consists of D_2O (99.5% enriched) made conducting by the addition of LiOD. Fleischman and Pons observed an abnormal energy release and neutron emissions from the positive palladium electrode; however, the Jones's group observed only the neutron emissions and no major energy release. As of today, more than fifty laboratories around the world have tried to duplicate the experiment using a similar arrangement. Unfortunately, most do not confirm the reported

results. Recent calculations [15] based on neutron tunnelling suggest that the rate for D-D cold fusion is roughly 3×10^{-64} per deuteron pair per second. This calculation has not yet been confirmed experimentally.

While neither the complete experimental facts of the situation nor an adequate theoretical model for such processes are currently available, it seems that the formation of high concentrations of deuterium nuclei in the palladium metal could be a prerequisite for the cold fusion process. At the University of Manitoba Accelerator Centre, several experiments involving the direct implantation of deuterium nuclei into metal surfaces were performed, based on the above assumption. The motivation was to investigate the results of the Fleischman and Pons electrolysis experiment in a similar non-equilibrium situation that did not involve heavy water (D_2O) as an intermediate material.

2.2 Ion Implantation with the Narodny Ion Accelerator

The process of implantation of 60 keV D_2^+ and D^+ ions into the palladium was carried out using the Narodny Ion Accelerator (NIA). The schematic diagram of the NIA is shown in Figure 2.2.1. The ion source is a duoplasmatron type, capable of producing positive ions of the feed gas which may then be accelerated to energies between 30 and 120 keV. Because the beam is created by an electrical discharge, both D_2^+ and D^+ (with estimated ratio $D_2^+:D^+ = 2:1$) ions populate the plasma and are extracted from the ion source and accelerated by a 60 kV potential difference. Upon hitting the target, a D_2^+ ion dissociates into two 30 keV D^+ ions.

Three different samples [(Pd-In), In, (Pd-C-In)] were mounted on the target holder and then subjected to bombardment by the D_2^+ and D^+ ions for an period of time. In each case, the implanted surface was that of the first element listed, namely Pd, In and Pd.
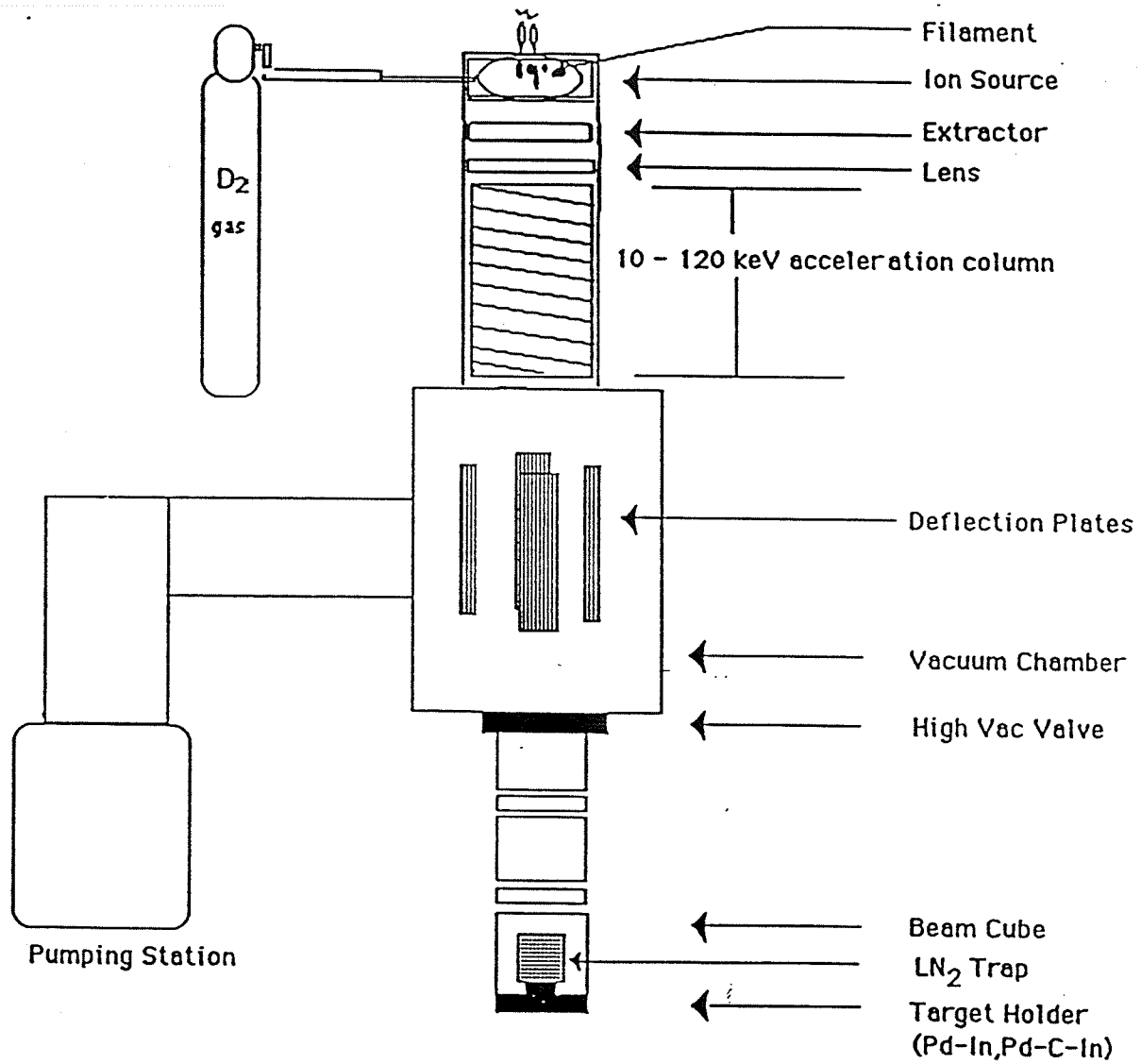
Figure 2.2.1   Schematic diagram of the Narodny Ion
                Accelerator.

2.3 Neutron Detection

Because of the importance of the observation of neutrons
for the identification of the fusion process, several
different detection methods were selected to indicate their
presence.

2.3.1 The Online Neutron Monitor (ONM)

The schematic layout of the ONM detection system is
shown in Figure 2.3.1, it registered data continuously during
the operation of the experiment. The detector was a 33.5 cm
long by 11.5 cm diameter cylindrical piece of NE102 plastic
scintillator with two RCA 4522 photomultiplier tubes (PMTs)
optically coupled to the ends. Plastic scintillator was
chosen as the active medium because it contains a large
concentration of hydrogen atoms. A neutron is detected by
scattering off the proton in the hydrogen atom, transfering
up to half of its energy to the proton. The plastic
scintillator also has a low average atomic number which
results in Compton scattering being the primary method of
detection of γ-rays. Thus, neutrons are elastically scattered
from the protons in the hydrogen atoms as they pass through
the plastic; and the slowing of the energetic protons
produces scintillation light. The scintillation light then

travels through the plastic to the PMTs where it is collected and converted to electronic pulses.

The electronic pulses from the PMTs were divided and one pulse from each is sent to one of two constant level discriminators. These discriminators were set to levels above the electronic noise level from the PMTs. Logic pulses from the discriminators were used to start a coincidence unit. Thus, a valid event required signals to be present in both PMTs. The coincidence pulse was used to monitor the number of events on a CAMAC scalar and provide a gate pulse for a LeCroy 2249A CAMAC analog-digital converter (ADC). The second of the PMT pulses from each tube was delayed so as to arrive at two channels of the ADC during the 200 nsec wide gate pulse. A 60 Hz pulser was fed into another CAMAC scalar unit to be used as a run-time clock for the experiment. A voltage level ADC was also incorporated into the system in order to monitor the beam current on the target through a 68 $k\Omega$ resistor. The CAMAC electronics and run-time event processing were controlled with a PC/XT compatible computer. For every valid event, the time of the event as recorded by the CAMAC scalar, the beam current, and the ADC values from both PMTs were recorded and written to disk. In this manner the presence of coincidence events was logged throughout the experimental runs. Analysis of these events could be carried
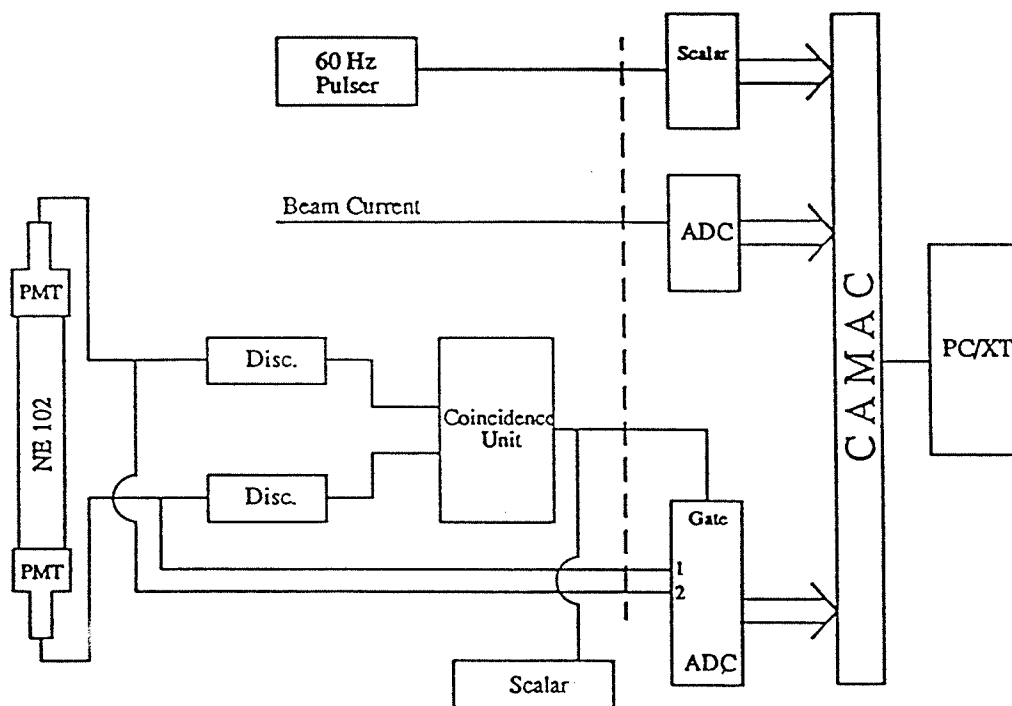
Figure 2.3.1   Schematic layout of the ONM detection system.

out offline at a later time.

2.3.2 Neutron Induced Activity

A way of measuring total neutron flux is through
activity induced by the neutron bombardment of a stable
element. In this technique, a sample is exposed to a neutron
flux for a measured period of time, creating a number of
radioactive nuclei. The sample is then placed in a low
background environment where the induced activity is measured
over a period of several halflives of the radioactive isotope
formed.

In this experiment, indium was selected as the suitable
element because of its identifiable gamma ray from a
metastable state of relatively short halflife. The principal
nuclear reaction of interest is:

$$^{115}In(n,n')^{115m}In \ \texttt{-------}> \ ^{115}In_{gs} + \gamma.$$
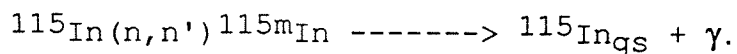
The effective threshold for this induced reaction is 1.4 MeV
and the cross section is approximately 2×10^{-29} m^2 for 2.45
MeV incident neutrons [16]. ^{115m}In has a halflife of 4.5 hrs
and its decay to the ground state of ^{115}In includes the
emission of a 0.336 MeV gamma ray 95% of the time [17].

2.3.3 Run-Time Monitors

Two additional broad spectrum neutron monitors, a Bonner sphere neutron survey meter (Snoopy NP-2) and Ludlum 12-4 neutron monitor were used to monitor the neutron fluxes at some distance from the site of the experiment. The monitors were calibrated for sensitivity to 2.5 MeV neutrons, and were used to observe possible rapid increases in neutron production which might represent a hazard.

The positions of the various detectors relative to the target are shown in Figure 2.3.2. These three different types of neutron monitor ensure over-determination of the presence of neutrons in this experiment.
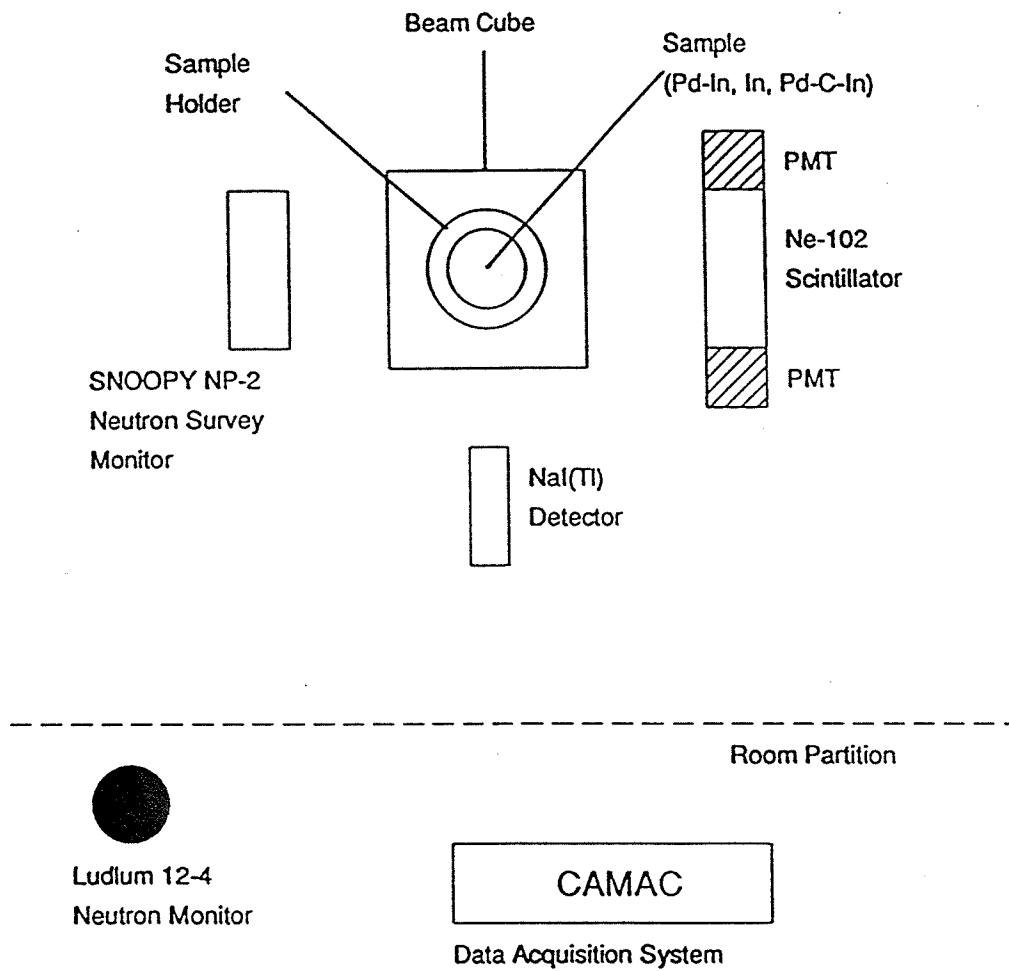
Figure 2.3.2   Positions of various neutron detectors
                relative to the target.

2.4 Procedure

In this experiment, a 0.2 mm thick metal target was bombarded with a stream of 60 keV D_2^+ and D^+ ions. The D_2^+ molecules dissociated into deuterium nuclei upon striking the target and eventually stop with a range of roughly 0.4 μm inside the palladium metal. To the extent that they are mobile, the deuterons distributed themselves throughout the palladium. A 10 hrs exposure to the deuterium beam corresponds to an implantation of roughly 10^{19} deuterons into the palladium metal. Assuming that all deuterons are retained in the palladium sample, they become targets themselves for the subsequent incoming deuterium nuclei.

The experiment consisted of three different experimental runs. In the first experiment (Pd-In), a 1 cm^3 indium pellet was placed under the palladium sheet target. The palladium was then implanted with deuterons for 24 hrs. The second experiment (In) involved the direct implantation of deuterons into a 4 mm thick indium sample. The purpose of the second experiment was to examine if any different effect would result from the implantation of a different metal. In the third experiment, a 3.3 mm thick carbon sheet was sandwiched between the palladium sheet and a second 4.8 mm thick indium pellet, to absorb any deuterons that might not have stopped

within the palladium. The implantation times for the second
and third experiment were 9 hrs and 13.5 hrs respectively.

The activated indium sample was removed from the target
holder immediately after the deuterium beam was turned off.
The sample was then taken to experimental area A of the
cyclotron laboratory where a NaI(Tl) detector and
multichannel analyser were located. The emission spectrum of
the indium sample was then measured for 9 hrs on each
occasion and the data were stored every hour throughout the
counting period. The energy spectrum was calibrated using
^{133}Ba, ^{22}Na and ^{137}Cs sources. A least square fit to the
calibration data indicated no significant deviation from
linearity. Background was counted for approximately 9 hrs
for each of the three experimental runs. Figure 2.4.1 shows
a typical background spectrum obtained using the NaI(Tl)
detector.

The sensitivity of the ONM detector to a neutron source,
gamma rays and cosmic rays was examined prior to the
experimental runs. The ONM detector was placed near the
Narodny accelerator. An Ac-Be neutron source was then placed
near the centre of the plastic scintillator and the resulting
pulse height spectrum obtained from the ONM detector is shown
in Figure 2.4.2. The gamma ray sensitivity of the ONM
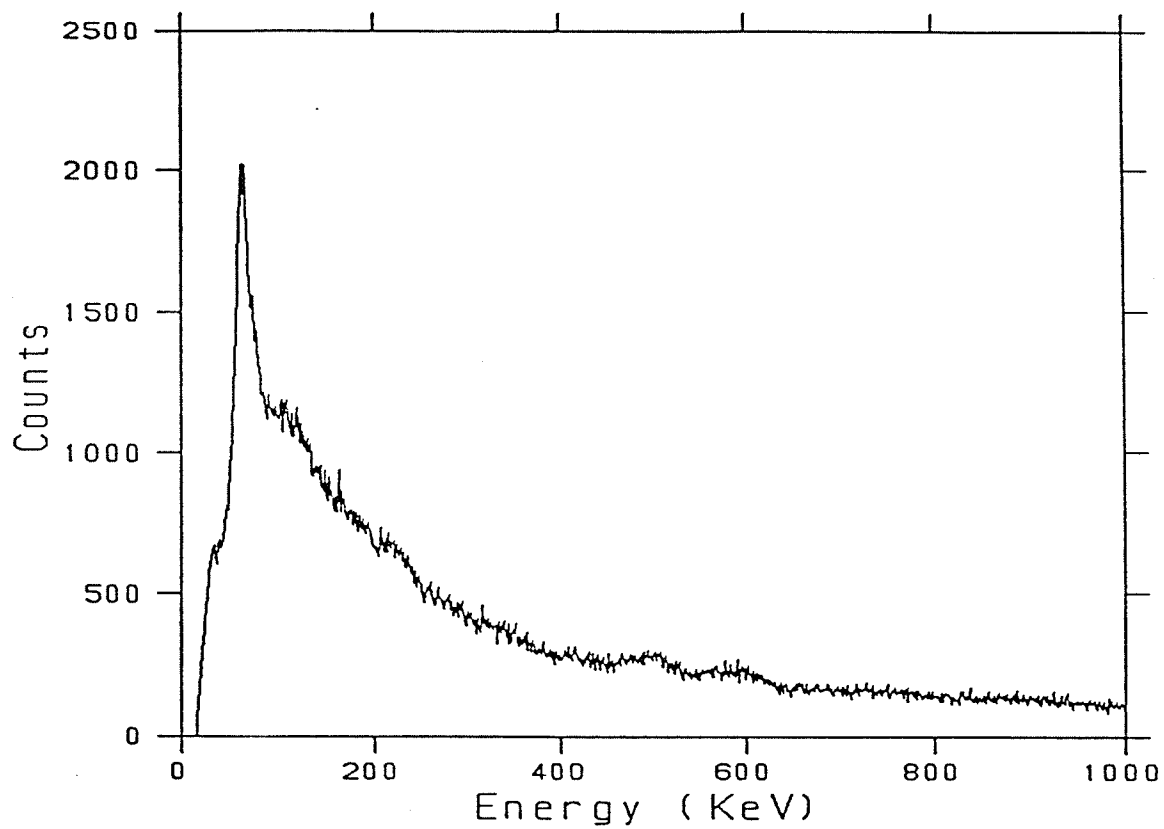
Figure 2.4.1   Typical background spectrum obtained from the
                NaI(Tl) detector.

Figure 2.4.2   Response of ONM detector to Ac-Be neutron
source.

detector was low when exposed to a 37 MBq ^{22}Na source. The response of the ONM detector due to cosmic rays was examined over a period of 14 hrs. Figure 2.4.3 shows the pulse height spectrum of the cosmic ray particles accumulated over this period of time.

Figure 2.4.3   Response of ONM detector to cosmic rays over
a period of 14 hrs.

2.5 Results and Analysis

2.5.1 The ONM Detector

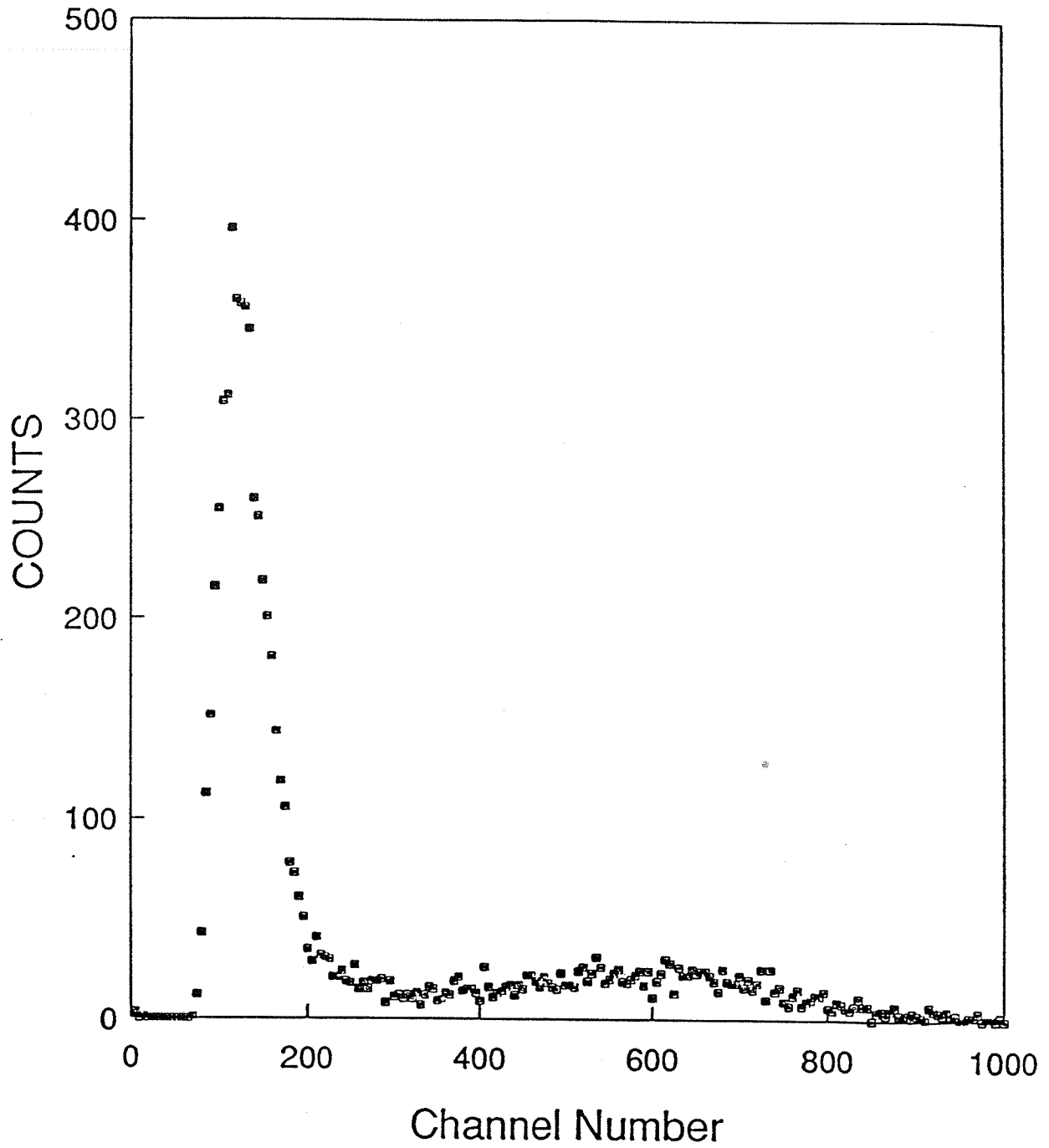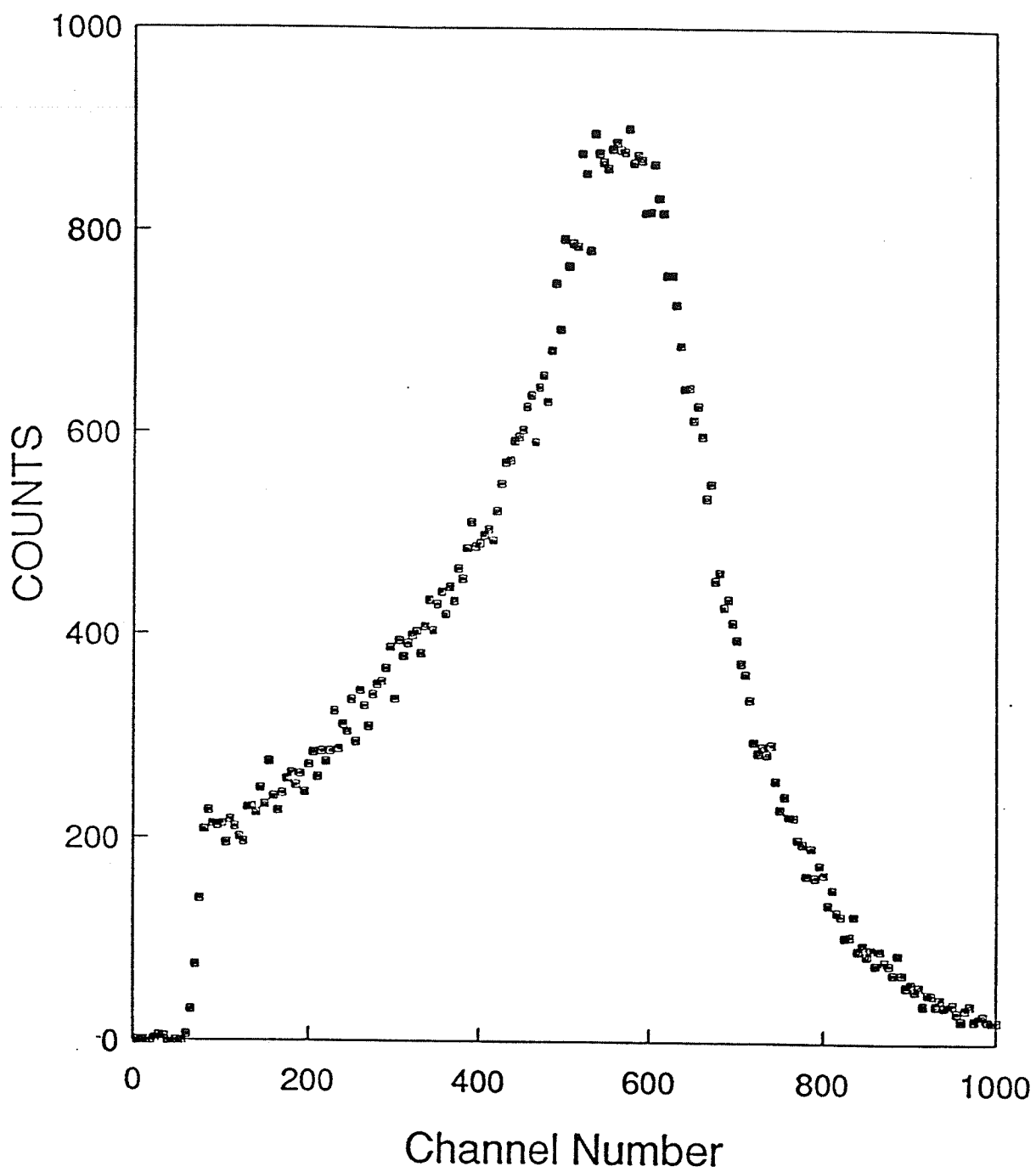The beam current monitor reading for the Pd-In experiment is shown in Figure 2.5.1. The average current was 11754 counts for the Pd-In experiment, and 15503 counts and 14019 counts for the In and Pd-C-In experiments respectively. The calibration scale was 3172 counts per volt across the 68 kΩ resistor.

Figure 2.5.2 shows the pulse height spectrum recorded during the Pd-In experiment. Consider the pulse height spectra shown in Figure 2.4.2 and 2.4.3. The main response of the ONM detector to the neutron source was below channel 300 while the response due to cosmic ray particles was largely above channel 300. For the purpose of analysis, channel 300 was chosen to divide the response of the ONM detector. The events with pulse heights below 300 will be referred to as 'neutron-like' or n-like events and those events that were above channel 300 are called 'minimum ionizing particle-like' or mip-like events.

The raw data registration rate obtained from the ONM detector for the Pd-In run is shown in Figure 2.5.3, where
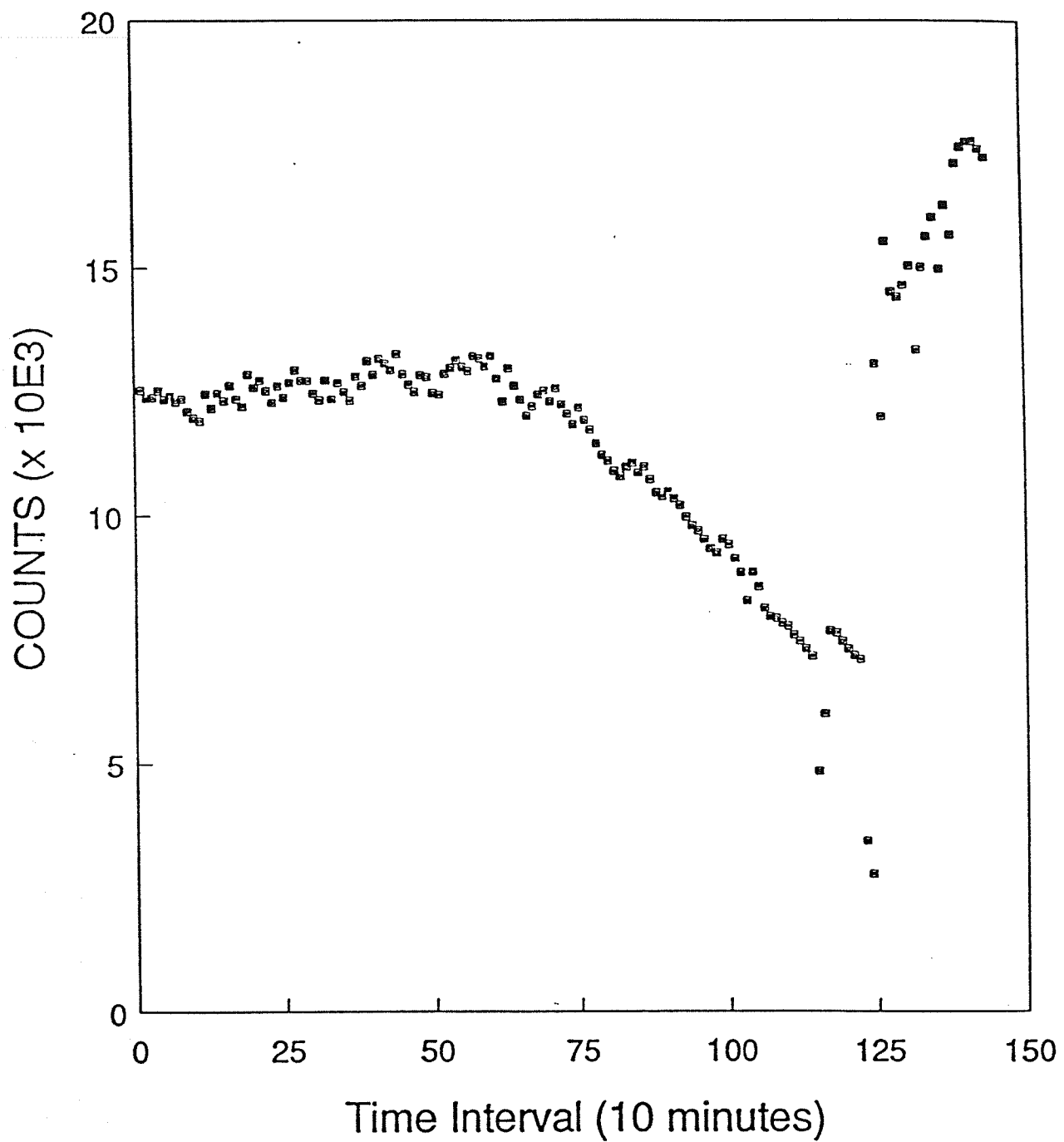
Figure 2.5.1   Beam current monitor reading for the Pd-In
                experiment.
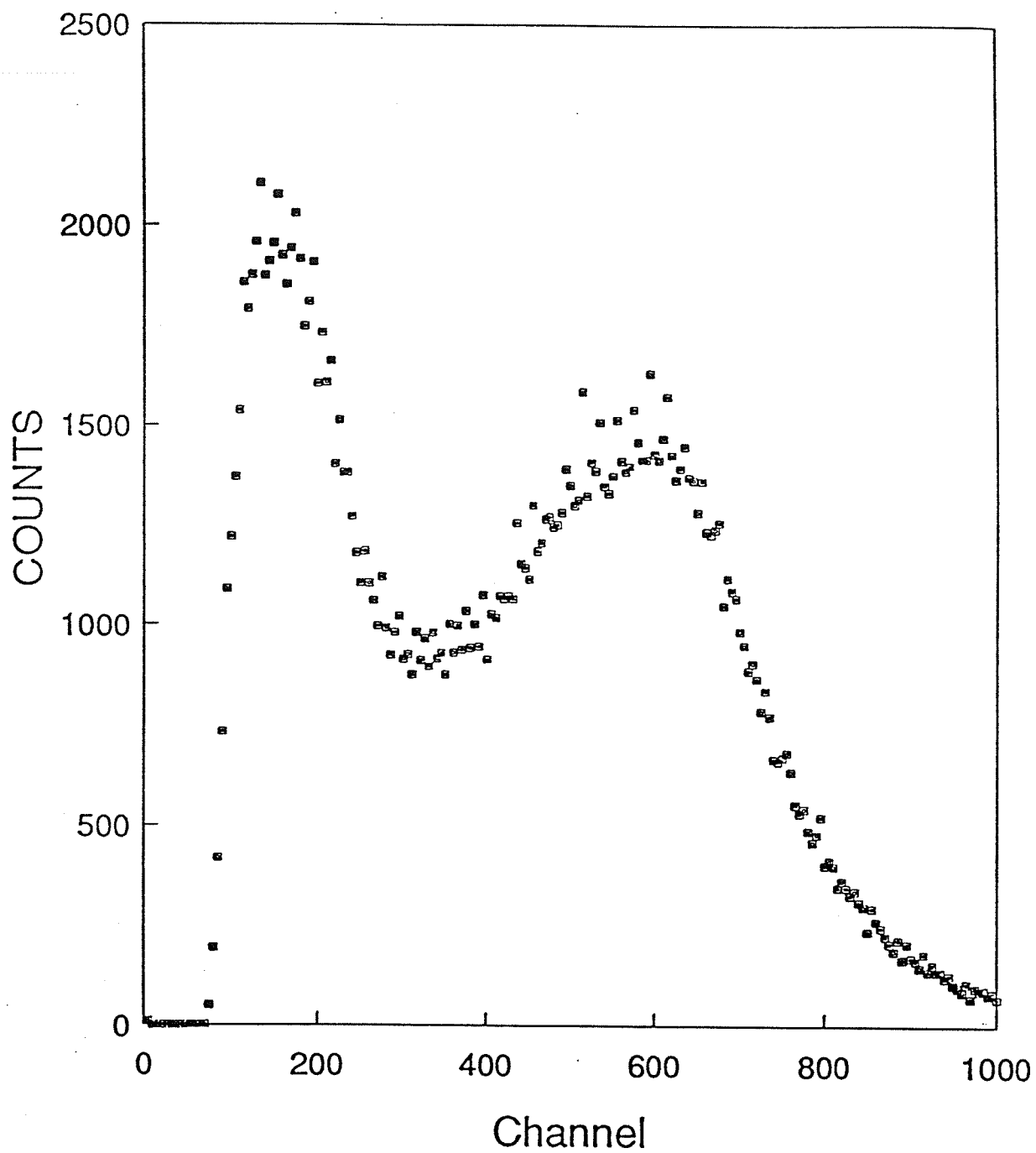
Figure 2.5.2   Pulse height spectrum recorded from the ONM
for the Pd-In experiment.
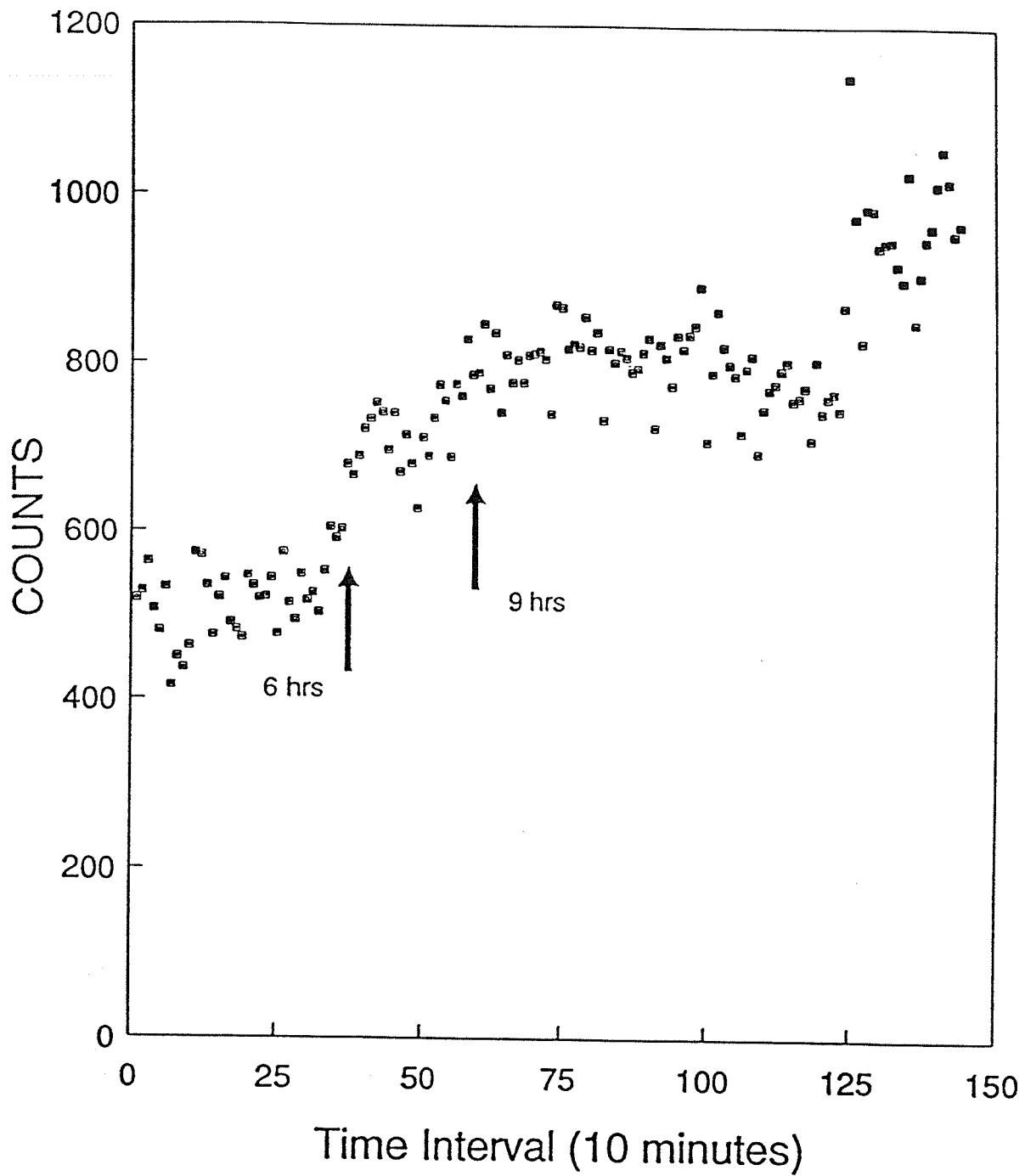
Figure 2.5.3   Raw data registration rate obtained from the
                ONM detector for the Pd-In experiment.

the run time has been subdivided into 10 minute intervals. There was a jump in the data registration rate 6 hrs into the experimental run. This increase seems to be associated with the ONM detector 'settling in' because it occurs simultaneously in both n-like and mip-like signals. The features occuring at 20 hrs into the run seem to be related to the rapid changing of beam current. Figure 2.5.4 shows the beam current corrected n-like signals from the Pd-In run. It is clear that there was a linear increase in the n-like signals with the experimental run time. No observable increase in the n-like signals was recorded during the first 6 hrs. The raw data for the mip-like signals is shown in Figure 2.5.5. As expected, the mip-like event registration rate remain roughly constant throughout the experimental run and is not expected to depend on the concentration of deuterium atoms present in the palladium nor the beam current.

Because the PMTs of the ONM detector were accidentally exposed to light after the completion of the Pd-In experiment, the ONM detector was rebuilt with new PMTs. The raw data registration rate for the In and Pd-C-In experiments are shown in Figure 2.5.6 and Figure 2.5.7 respectively. The data registration rate jumps observed during these two experimental runs were characterized by no measurable signal

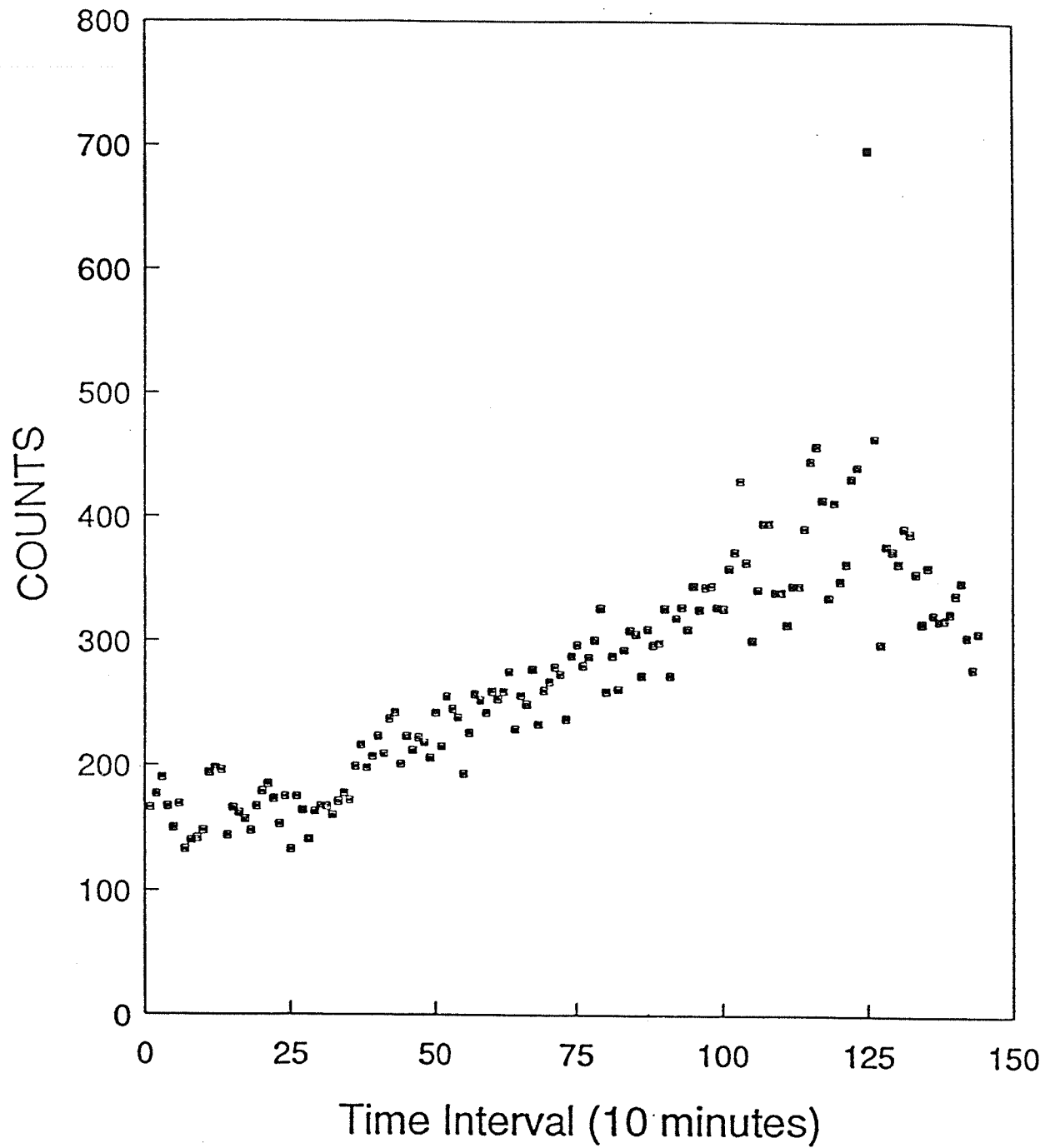Figure 2.5.4   Beam current corrected n-like signals
                 registration rate from the Pd-In experiment.
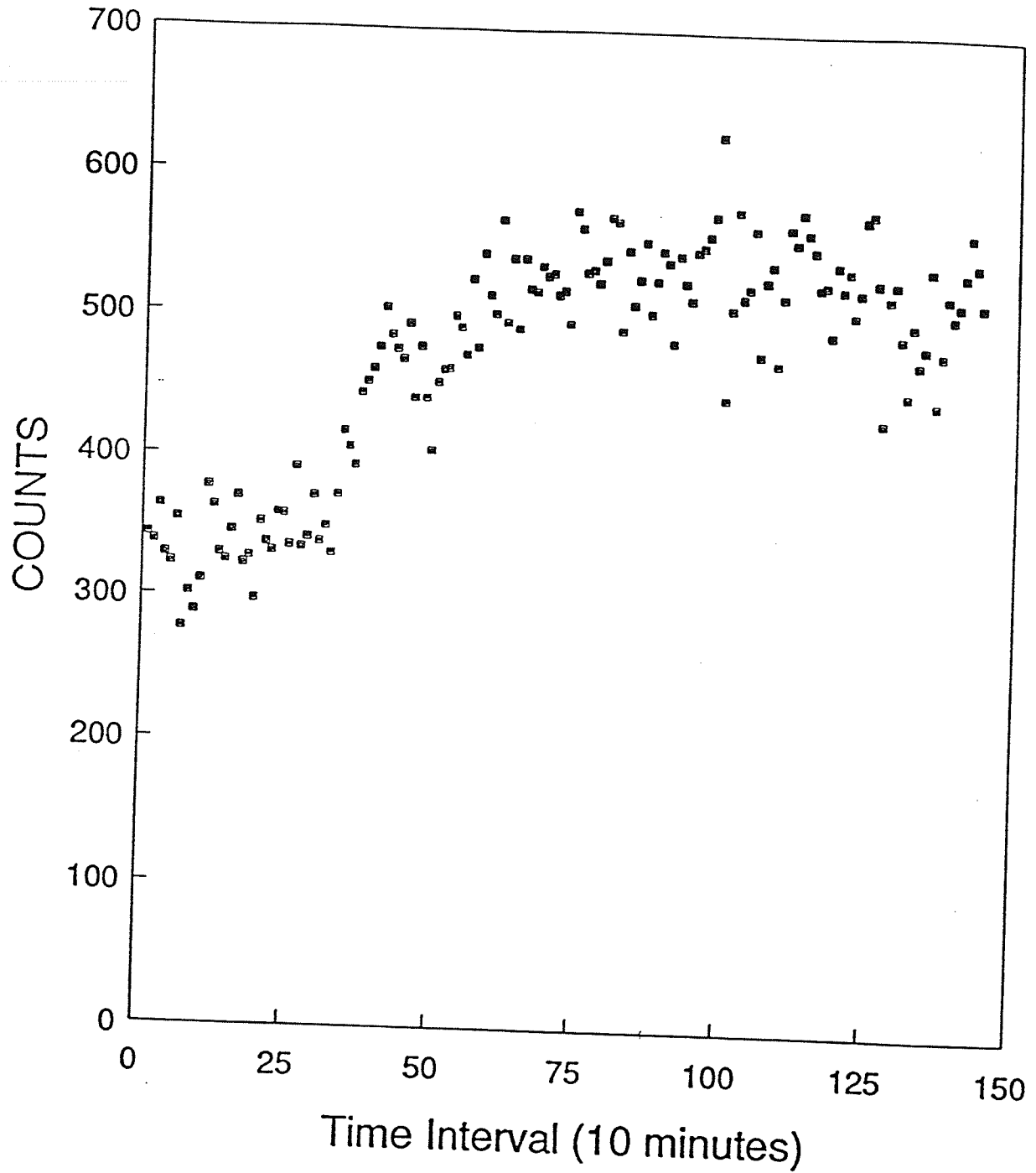
Figure 2.5.5   Raw data registration rate for the mip-like
                signals during the Pd-In experiment.
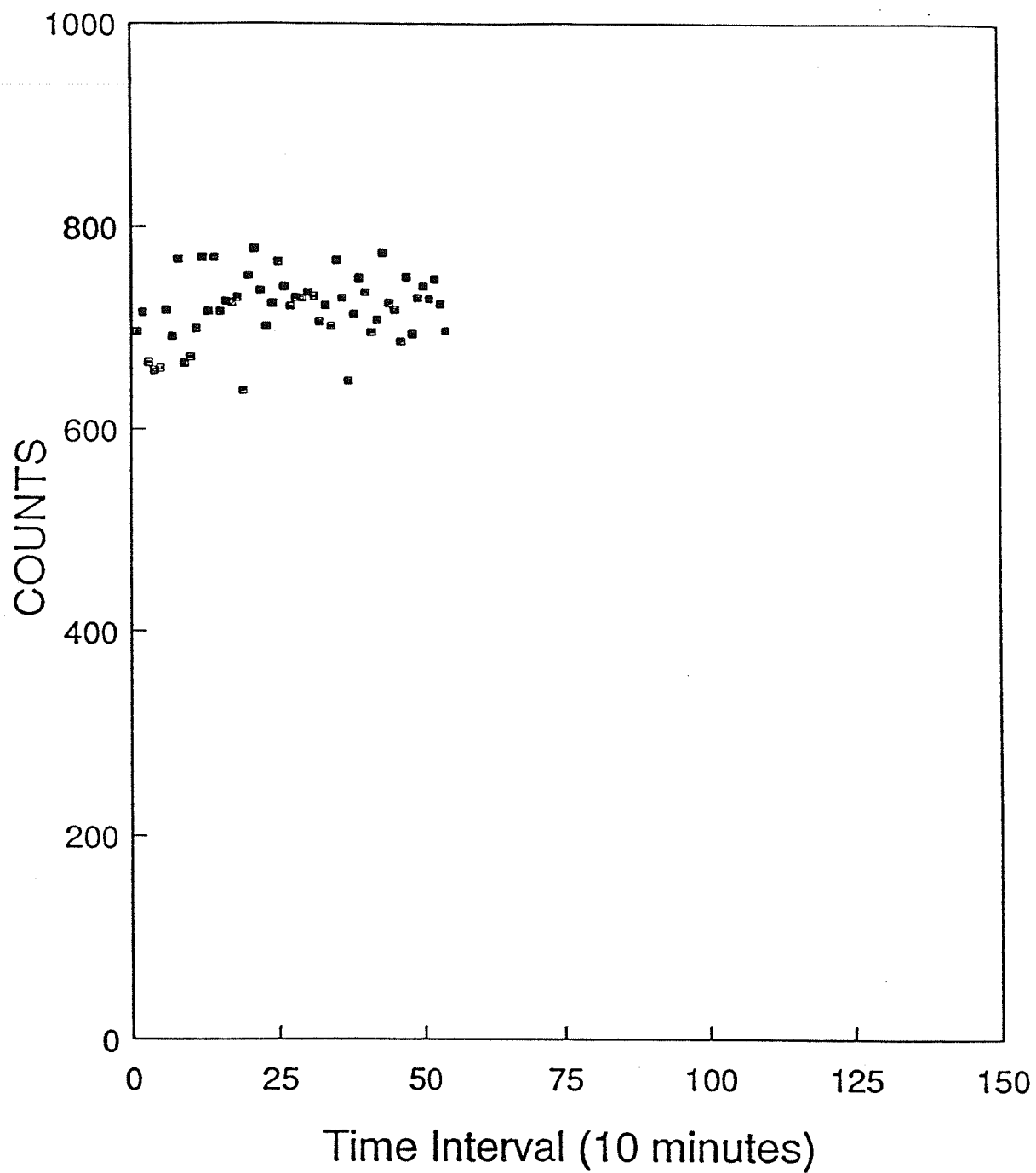
Figure 2.5.6   Raw data registration rate from the In
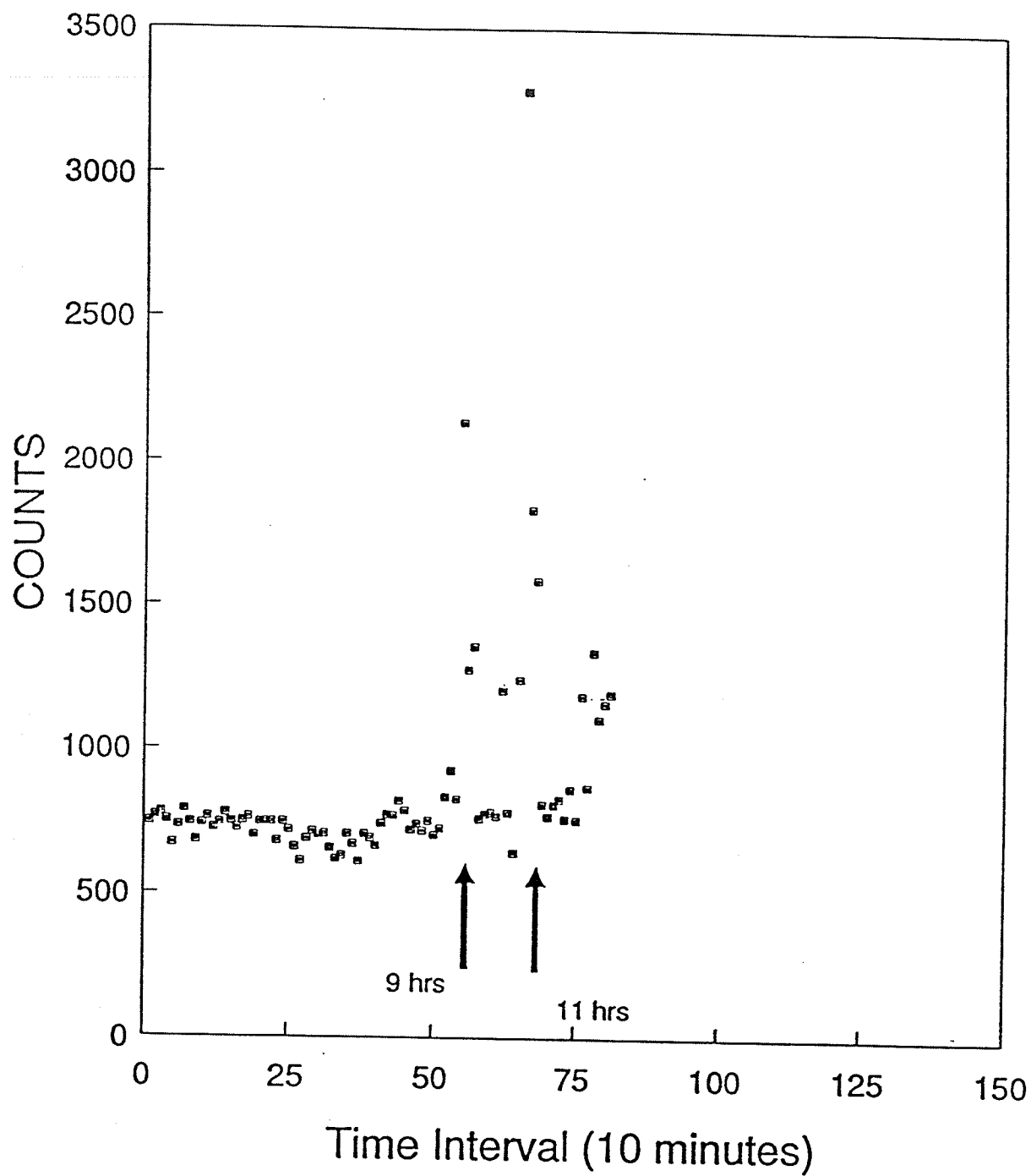   experiment.

Figure 2.5.7   Raw data registration rate from the Pd-C-In
                experiment.

from the ONM detector. This could have been a result of inproper calibration of the new PMTs or possibly the data registration rates were too high and may exceeded the maximum data registration rate allowed by the monitoring equipment. Table 2.5.1 gives the total number of events recorded from the ONM detector for the three different experimental runs.

Table 2.5.2 summarizes the raw and beam current corrected data registration rate for 10 min time interval in the three series of experiments. Note that the mip-like event registration rate is roughly constant over all experimental runs. The estimated energy of the neutrons generated for this experiment is roughly 1 to 3 MeV and the neutron production rate is roughly 800 neutrons per second.

2.5.2   Indium Activation

Figure 2.5.8 (a), (b), (c) show the background subtracted energy spectrum of the activated indium obtained from each of the experimental runs. For the Pd-C-In experiment, a gamma ray peak with centroid at energy (331.3 +/- 10.0) keV is clearly observed. The halflife of the activated indium was calculated to be (4.58 +/- 0.12) hrs. Both the observed gamma ray energy and the halflife of the excited indium correspond to those expected from a

Experimental Run	Average Beam Current (x 10E-6 A)	Live Time (Hour)	Total Number of Events
Pd-In	58.2	24	10 6353
In	75.6	8.83	3 9014
Pd-C-In	68	13.5	7 0245
Cosmic Rays	-	14	7 3013

Table 2.5.1   Total number of events obtained from the
ONM detector for the three different
experimental runs.

Experimental Run	n-like Event Rate per 10 minute interval		mip-like Event Rate per 10 minute interval
	unnormalized	normalized	unnormalized
Pd-In	266	272	502
In	300	319	685
Pd-C-In	413	422	673
Background	–	–	604

Table 2.5.2   Raw and beam current corrected data registration
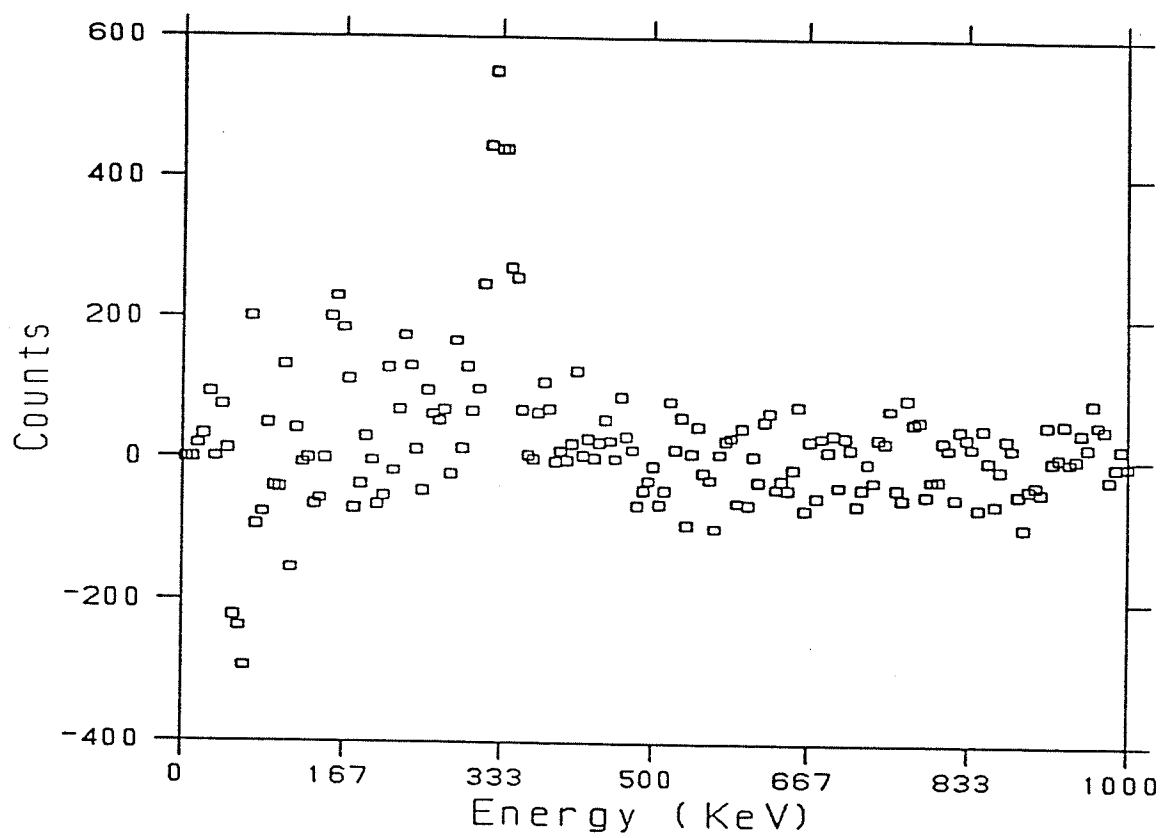rates in the series of three experiments.

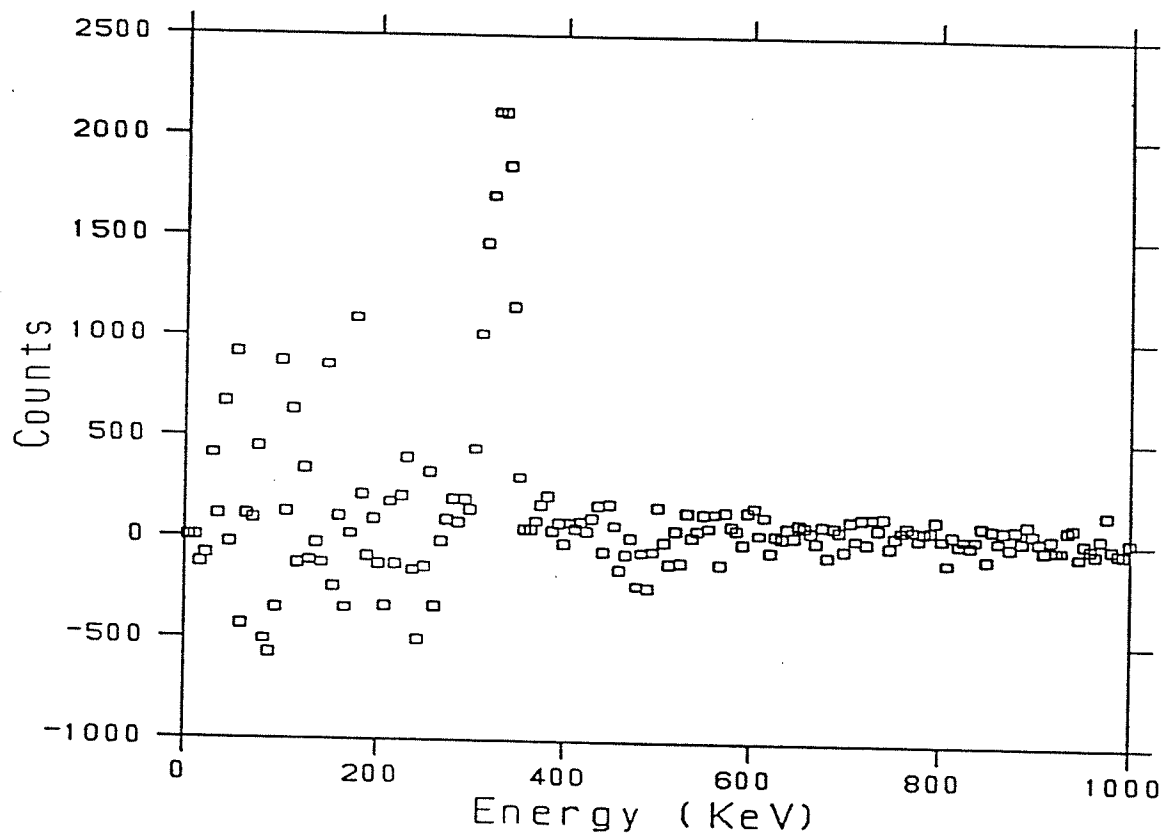Figure 2.5.8a   Background subtracted ^{115m}In energy spectrum
for the Pd-In experiment.

Figure 2.5.8b   Background subtracted ^{115m}In energy spectrum
for the In experiment.
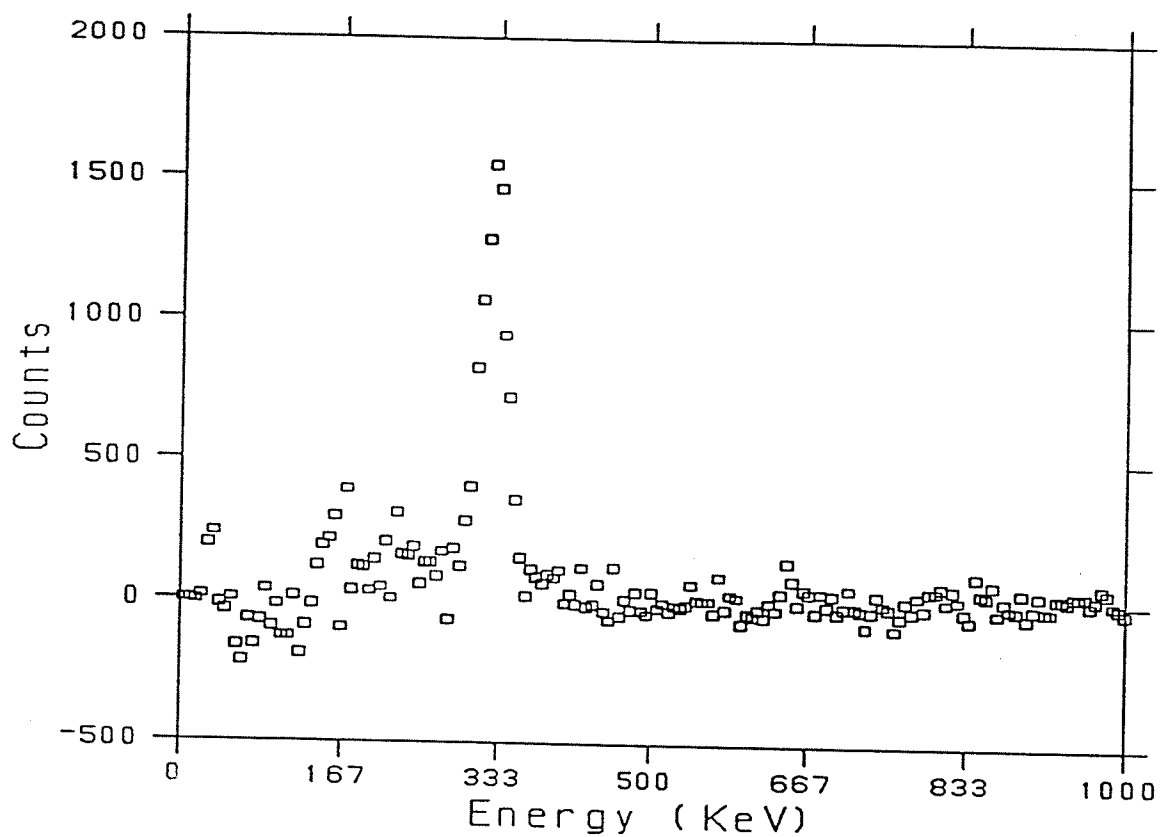
Figure 2.5.8c   Background subtracted ^{115m}In energy spectrum
for the Pd-C-In experiment.

$$^{115}In(n,n')^{115m}In \longrightarrow ^{115}In_{gs} + \gamma$$
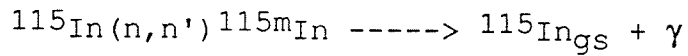
reaction. This fact indicates that a significant neutron
flux was generated during the period of implantation of
deuterium nuclei into the palladium. The results obtained
from all three experiments are summarized in Table 2.5.3.

Note that the

$$^{115}In(n,n')^{115m}In \longrightarrow ^{115}In_{gs} + \gamma$$
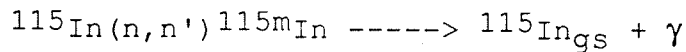
reaction also occurred in the second experiment where the
deuterium nuclei were implanted directly into the indium
pellet. A larger degree of neutron activation was expected
and observed compared to the Pd-In and Pd-C-In runs; since
the indium acted as both the target for the deuterium beam
and the detector of subsequent neutrons.

Using the data obtained in studying the decay of the
^{115m}In, the neutron rate generated in the experiment was
estimated to be of order of 1×10^3 neutrons per second,
assuming that the neutron production rate is constant.

Experiment	Gamma Energy (keV)	Halflife (Hour)	Peak Area (x 10E4)
Pd-In	333.5+/-10.6	4.53+/-0.96	3.84+/-0.20
In	331.6+/-9.3	4.31+/-0.17	8.45+/-0.37
Pd-C-In	331.3+/-10.0	4.58+/-0.12	7.84+/-0.22

Table 2.5.3   Total number of gamma rays detected from the activated indium during the three experiments.

2.6 Theoretical Estimation of Neutron Production Rate

2.6.1 Direct Calculation of 'Hot' Fusion Reaction Rate

Since this experiment involved the implantation of palladium by 60 keV and 30 keV D^+ ions, these ions can react with the deuterons already implanted at various depths inside the palladium metal.

The total cross-section σ, of the D-D nuclear reaction as a function of incident D^+ energy has been experimentally determined [18] and is given by

$$\sigma(E) = (2.88 \times 10^{-22} / E) \, \text{Exp} \, [-45.8 / (E)^{0.5}] \qquad [\text{cm}^2].$$

Similarly, the ratio of $D(d,n)^3\text{He}$ cross-section (σ_{DDn}) to $D(d,p)T$ cross-section (σ_{DDp}) was previously measured to be

$$\sigma_{DDn}(E) = (6 \times 10^{-4} E + 0.927) \, \sigma_{DDp}(E)$$

The energy of the deuterons as they traverse the palladium has been calculated and is shown in Figure 2.6.1 [19]. Because of the energy losses, the D-D fusion reaction rate varies at various depths x inside the palladium; since
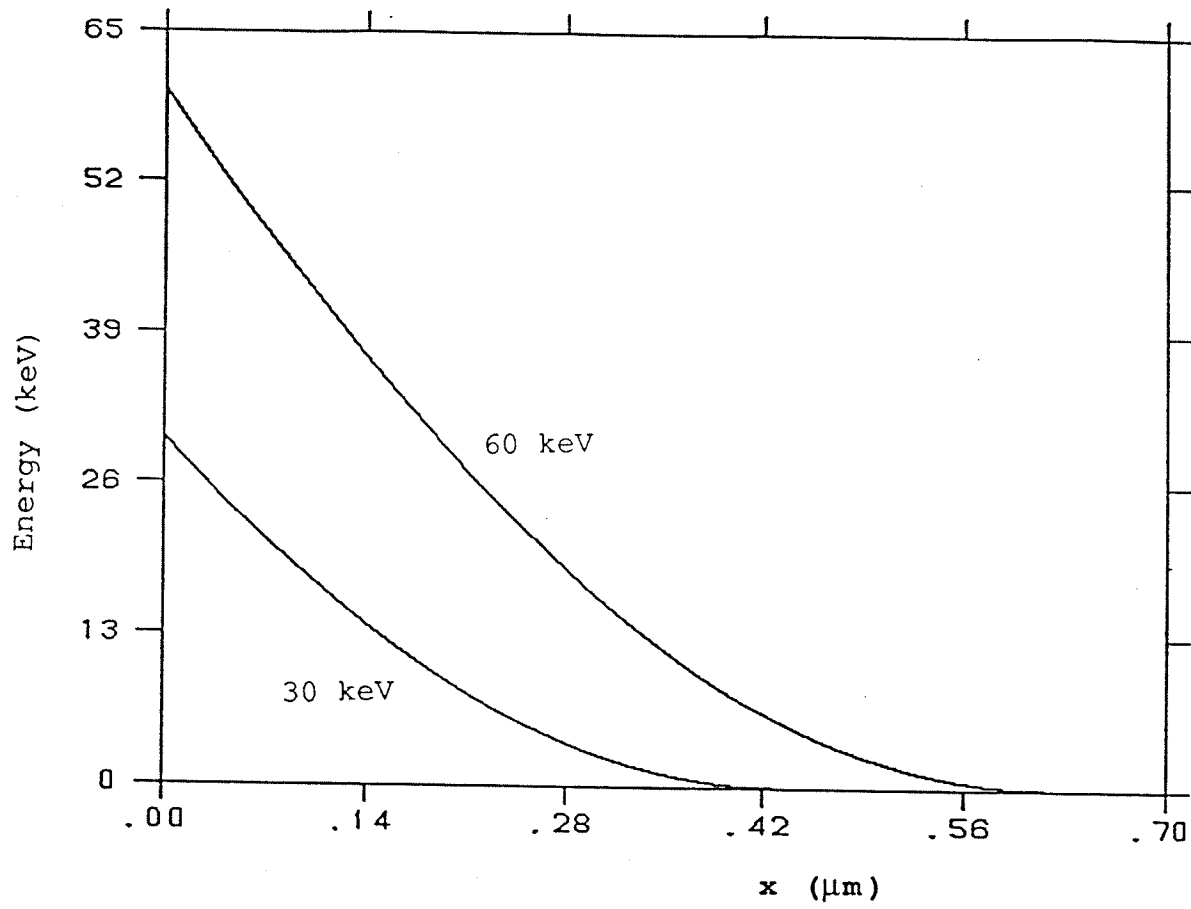
Figure 2.6.1   Energy of deuterons as a function of depth x
inside the palladium metal.

the incident deuteron energy is now an explicit function of the depth x. Figure 2.6.2 shows the cross-section σ_{DDn} for deuterons of energy appropriate to the depth x, at various depths x for the 60 keV incident D^+ ions. Since the 30 keV D^+ ions have a total range less than that of 60 keV D^+ ions, most of the 60 keV D^+ ions will interact with the 30 keV D^+ ions implanted in the palladium metal.

Assuming that all the implanted deuterons were retained in the palladium metal, and that the distribution of these deuterons inside the palladium metal is approximately a Gaussian function,

$$N(x,t) = [N_O(t) / (2\pi)^{0.5} \alpha] \, Exp \, [-(x - R_O)^2 / 2 \, \alpha^2]$$

where R_O is the mean range of the implanted deuterons, α is the deviation from R_O determined from range straggling and $N_O(t) = \phi t$ is the number of implanted deuterons. ϕ is the implantation rate of incident 30 keV D^+ ions and t is the implantation time. The total reaction rate can then be estimated by integrating the differential reaction rate over the total path range R_T of the 30 keV D^+ ions, i.e.

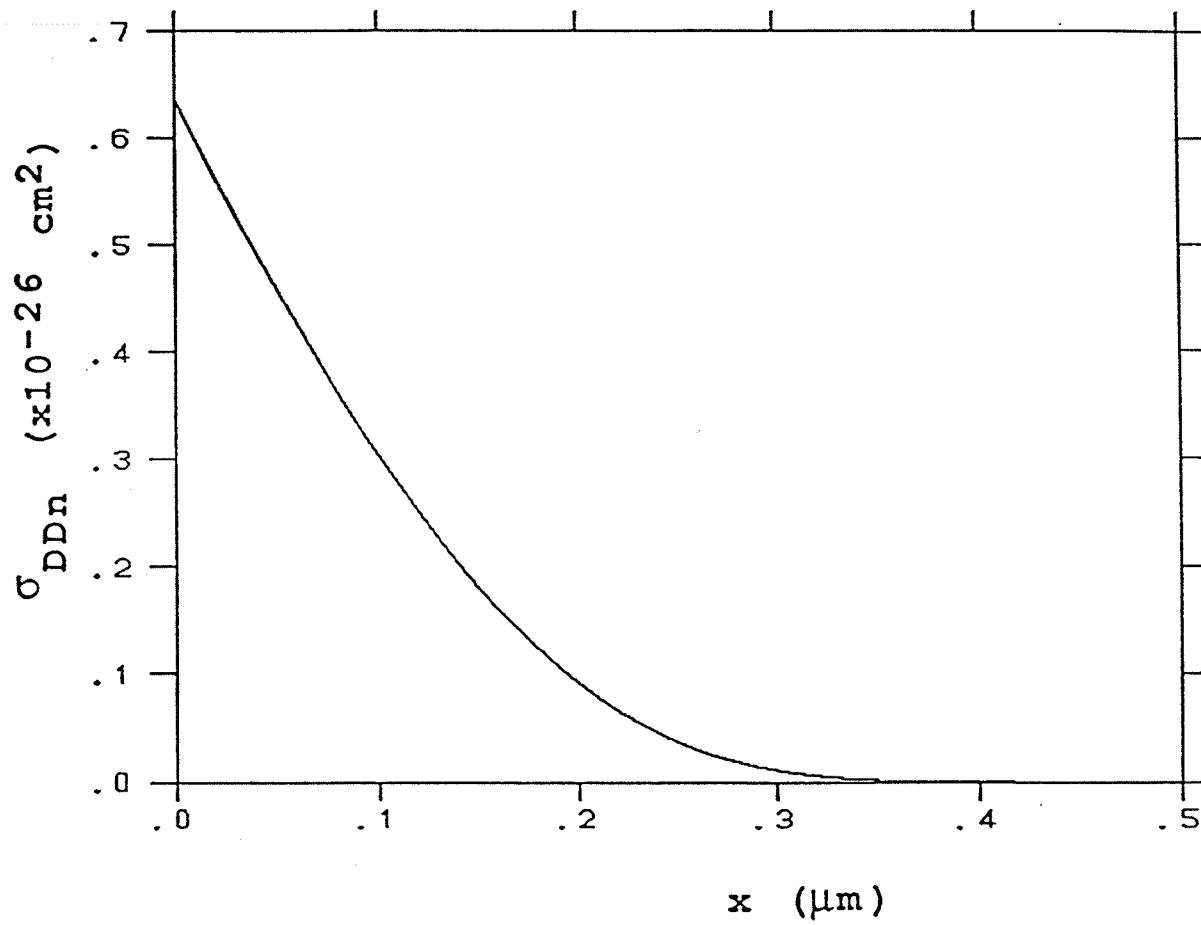$$Rate(t) = \int_0^{R_T} \Phi \, \sigma_{DDn}(x) \, N(x,t) \, dx$$

Figure 2.6.2   The variation of cross-section σ_{DDn} with x

for the 60 KeV incident D^+ ions.

where Φ is the flux of incident 60 keV D^+ ions.

The total reaction rate is time dependent since the number of implanted deuterons $N_O(t)$ increases with time. Note that the calculation does not include a component arising from incident 30 keV D^+ ions interacting with the implanted deuterons. This is because the reaction cross-section for 30 keV deuterons is roughly 1/5 of that for 60 keV deuterons, and decreases rapidly as the deuteron energy decreases (x increases). Although $N(x,t)$ is a Gaussian function, the rapid decrease in the reaction cross-section dominates the product $N(x,t)\sigma_{DDn}(x)$ so that the overall reaction rate remains small compared to reaction rate generated from incident 60 keV D^+ ions.

The following numbers were used to calculate the total reaction rate for the Pd-In experiment:

$\phi = 4.84 \times 10^{14}\ D^+/sec$

$\Phi = 2.98 \times 10^{13}\ D^+/sec\ cm^2$

$\alpha = 0.035\ \mu m$

$R_T = 0.43\ \mu m$

$R_O = 0.23\ \mu m$

and the resulting total reaction rate, which is also the rate of neutron production, is

$$Rate(t) = 1.09 \times 10^{-2}\ t \quad [neutron/sec].$$

Therefore for the Pd-In experiment (24 hrs), a total of 3.41×10^7 neutrons were produced. Taking into account the solid angle subtended by the indium pellet, roughly 30% of 3.41×10^7 neutrons would cause the production of ^{115m}In nuclei.

2.6.2 Calculation of the Number of Induced Indium Nuclei

During the irradiation, the growth of ^{115m}In nuclei is proportional to the activation cross-section σ_a, the neutron flux ϕ_n and the number of indium atoms N_i. However, the ^{115m}In nuclei decay during the irradiation process at a rate $\lambda N_a(t)$, where λ is determined by the decay constant of ^{115m}In and $N_a(t)$ is the total number ^{115m}In nuclei present at any time t. Hence the net build-up rate of ^{115m}In is

$$dN_a(t)/dt = \phi_n \sigma_a N_i - \lambda N_a(t)$$

and $\quad \phi_n$ = [Rate(t)/Area] [Fraction of solid angle

subtended by the indium pellet].

Integrating the above expression yields

$$N_a(t) = A \sigma_a N_i [t/\lambda - 1/\lambda^2 + (1/\lambda^2)\exp(-\lambda t)]$$

where A = [1.09×10^{-2}/Area] [Fraction of solid angle

subtended by the indium pellet] for the Pd-In experiment,

$\lambda = 4.27 \times 10^{-5}$ sec^{-1} and $\sigma_a = 2 \times 10^{-25}$ cm^2. Table 2.6.1

summarizes the results obtained from this calculation for the

Pd-In and Pd-C-In experiments.

Experiment	Live Time (Hours)	Number of Activated Indium Nuclei Observed (x 10E4)	Number of Activated Indium Nuclei Calculated (x 10E4)
Pd-In	24	3.84 +/- 0.20	3.71
Pd-C-In	13.5	7.84 +/- 0.22	1.13

Table 2.6.1 The number of activated indium nuclei observed and

calculated for the Pd-In and Pd-C-In experiments.

2.7 Discussion

From the data obtained in this experiment, the estimated neutron production rate is 1×10^3 neutrons per second. One interesting feature to note is that from Figure 2.5.4, the number of neutron produced increases linearly with the implantation time. Therefore the neutron production rate is constant and independent of time. The calculation performed in section 2.6 is based on the assumption that the reaction rate is time dependent. However, the data obtained from the ONM detector does not show this feature. Also, from Table 2.6.1, although the observed number of ^{115m}In nuclei produced from the Pd-In experiment might seem to agree with the hot fusion calculation. However, the calculated number of ^{115m}In nuclei from the Pd-C-In experiment is only 15% of the observed value.

Several factors such as the diffusion rate of deuterons and the exact profile of the implanted deuterons inside the palladium metal at a given time were not included in the calculation of hot fusion reaction rate. It still remains a question as to how these factors would influence the overall hot fusion reaction rate.

2.8 Conclusions

A significant neutron flux is observed from the implantation of palladium and indium by 60 keV and 30 keV D^+ ions. The experimental data obtained from the ONM detector and the induced ^{115m}In experiment give consistent results. The estimated neutron production rate is roughly 1×10^3 neutrons per second for this experiment.

A preliminary calculation of the hot fusion reaction rate shows disagreement with the experimental data. In order to determine the role of cold fusion in this experiment, a further examination on the role of hot fusion, or a more detailed calculation of the hot fusion reaction rate is needed.

References

[1] J.S.C. McKee and G.R. Smith in Advanced in Electronics
     and Electron Physics; ed. P.W. Hawkes (Academic Press)
     73 (1989) 93.

[2] W.D. Ramsay, M.S.A.L. Al-Ghazi, J. Birchall and
     J.S.C. McKee, Phys. Lett. 69A (1978) 258.

[3] J.S.C. McKee, J.J.G. Durocher, N.M. Halden, D. Gallop,
     A. Mirzai, M.S. Mathur, G.R. Smith and Y.H. Yeo,
     Conference Proceedings, Invited talk to the IX
     International Conference on Ion Beam Analysis, June,
     1989, Kingston, Ontario, Canada. To be published in
     Nucl. Inst. Meths. in Physics Research.

[4] A.D. Dymnikov, T.Ya. Fishkova and S.Ya. Yavor, Sov.
     Phys-Tech. Phys. 10 (1965) 340.

[5] R. Nobiling, Y. Civelekoglu, B. Pouh, D. Schwalm and
     K. Traxel, Nucl. Inst. Meths. 130 (1975) 325.

[6] A. Papoulis, Systems and Transforms with Applications
     in Optics.

[7] K. Abdul-Retha, M.Sc. Thesis, University of Manitoba,
     (1987).

[8] F. WAtt, G.W. Grime, G.D. Blower, J.Takacs and D.J.T.
     Vaux, Nucl. Inst. Meths. 197 (1982) 65.

[9] J.S.C. McKee, G.R. Smith, Y.H. Yeo, K. Abdul-Retha,
     D.M. Gallop, J.J.G. Durocher, W. Mulholland and C.A.
     Smith, Nucl. Inst. Meths. in Physics Research, B40/41
     (1989) 680.

[10] G.J.F. Legge, D.N. Jamieson, P.M.J. O'Brien and A.D.
     Mazzolini, Nucl. Inst. Meths. 197 (1982) 85.

[11] G.W. Grime and F. Watt, Beam Optics of Quadrupole Probe-
     forming Systems.

[12] C. Dew van Siclen and S.E. Jones, J. Phys. G: Nucl.
     Phys. 12 (1986) 213.

[13] M. Fleischmann and S. Pons, J. Electroanalytical Chem.
     261 (1989) 301.

[14] S.E. Jones, E.P. Palmer, J.B. Czirr, D.L. Decker, G.L.
     Jensen, J.M. Thorne, S.F. Taylor and J. Rafelski, Nature

338 (1989) 737.

[15] S.E. Koonin and M. Nauenberg, Submitted to Nature, April 7, 1989.

S.E. Koonin, Submitted to Phys. Rev. Lett., April 19, 1989.

[16] International Commission on Radiation Units and Measurements, ICRU Report 26, Neutron Dosimetry for Biology and Medicine, Washington, D.C., (1977).

[17] C.M. Lederer and V S. Shirley, (Editors), Table of Isotopes, 7th Edition, Wiley-Interscience Publications, N.Y., 1978.

[18] W.R. Arnold, J.A. Phillips, G.A. Sawyer, E.J. Stovall,Jr and J.L. Tuck, Phys. Rev. 93 (1954) 483.

[19] Hydrogen Stopping Powers and Ranges in All Elements, H.H. Andersen and J.F. Ziegler, Pergamon Press, 1977.